

1 **Land use and anthropogenic heat modulate ozone by meteorology:**
2 **A perspective from the Yangtze River Delta region**

3 Chenchao Zhan ^a, Min Xie ^{a,*}

4 ^a School of Atmospheric Sciences, CMA-NJU Joint Laboratory for Climate Prediction Studies,
5 Jiangsu Collaborative Innovation Center for Climate Change, Joint Center for Atmospheric Radar
6 Research of CMA/NJU, Nanjing University, Nanjing 210023, China

7 -----
8 * Corresponding author. minxie@nju.edu.cn (M. Xie)

9
10 **Abstract:** With the rapid advance in urbanization, land use and anthropogenic heat (AH) dictated
11 by human activities significantly modify the urban climate and in turn the air quality. Focusing on
12 the Yangtze River Delta (YRD) region, a highly urbanized coastal area with severe ozone (O₃)
13 pollution, we estimate the impacts of land use and AH on meteorology and O₃ using the WRF-Chem
14 model. These results enhance our understanding of the formation of O₃ pollution in rapidly
15 developing city clusters with place-specific topography, as most of our results can be supported by
16 previous studies conducted in other regions around the world. Regional O₃ pollution episodes occur
17 frequently (~26 times per year) in the YRD from 2015 to 2019. These O₃ pollution episodes are
18 usually in calm conditions characterized by high temperature (over 20 °C), low relative humidity
19 (less than 80%), light wind (less than 3 m s⁻¹) and shallow cloud cover (less than 5 okta). In this
20 case, O₃ pollution belts tend to appear in the converging airflows associated with the sea and the
21 lake breezes. On the other hand, rapid urbanization has significantly changed land use and AH in
22 this region, which subsequently affects the meteorology and O₃ concentration. The largest change
23 in land use comes from urban expansion, which causes an increase in 2-m temperature (T₂) by a
24 maximum of 3 °C, an increase in planetary boundary layer height (PBLH) by a maximum of 500 m,
25 a decrease in 10-m wind speed (WS₁₀) by a maximum of 1.5 m s⁻¹ and an increase in surface O₃ by
26 a maximum of 20 µg m⁻³. With regard to the sea and lake breezes, the expansion of coastal cities,
27 like Shanghai, can enhance the sea breeze circulation by ~1 m s⁻¹. During the advance of the sea
28 breeze front inland, the updraft induced by the front makes well vertical mixing of O₃. However,
29 once the sea breeze is fully-developed in the afternoon (~17:00 LT), further progression inland will

30 stall. Then O₃ removal by the low sea breeze will be weakened, and surface O₃ can be 10 μg m⁻³
31 higher in the case with cities than no-cities. The expansion of lakeside cities, such as Wuxi and
32 Suzhou, can extend the lifetime of lake breezes from noon to afternoon. Since the offshore flow of
33 the lake breeze transports high O₃ from the land to the lake, the onshore flow brings high O₃ back
34 to the land. Surface O₃ in lakeside cities can increase as much as 30 μg m⁻³. Compared to land use,
35 the effects of AH are relatively small. The changes mainly appear in and around cities where AH
36 fluxes are large. There are increases in T₂, PBLH, WS₁₀ and surface O₃ when AH fluxes are taken
37 into account, with increments of approximately 0.2 °C, 75 m, 0.3 m s⁻¹ and 4 μg m⁻³, respectively.
38 AH contributes largely to the urban environment, altering meteorological factors, O₃ concentration
39 and urban breeze circulation, but its effect on the sea and the lake breezes seems to be limited.

40 **Key Words:** ozone; local circulations; land use; anthropogenic heat; the Yangtze River Delta;

41

42 **1 Introduction**

43 Tropospheric O₃ is a secondary pollutant formed by a series of complex chemical reactions
44 (Chameides and Walker, 1973; Xie et al., 2014) of precursor gases such as nitrogen oxides
45 (NO_x=NO+NO₂) and volatile organic compounds (VOCs) in combination with sunlight. It has
46 received continuous attention within the last few decades due to its negative effects on human
47 respiratory system (Jerrett et al., 2009) and the growth of vegetation (Mills et al., 2011). The global
48 average lifetime of tropospheric O₃ is 20 to 25 days, and it will decrease to 5 days in the boundary
49 layer (Young et al., 2013). The relatively long lifetime of O₃ favors regional/long-range transport
50 and brings huge challenges to its control (Bergin et al., 2005). O₃ concentrations considerably
51 depend on weather conditions because they play an important role in determining the chemistry,
52 dispersion and removal of O₃ (Jacob and Winner, 2009). Elevated O₃ usually occurs under warm
53 dry weather with strong sunlight, high temperature, low relative humidity and light wind speed
54 (Zhang et al., 2015). Furthermore, weather conditions have many similarities in certain weather
55 pattern (Buchholz et al., 2010; Zhan et al., 2019), and the main weather patterns associated with O₃
56 pollution episodes in China are tropical cyclones and continental anticyclones (Wang et al., 2017).

57 O₃ concentration and meteorology in urban areas are of great concern because urban areas have
58 huge populations. A report from the United Nations pointed out that 69.6% of the world's population
59 will live in cities by 2050. Because of historical and cultural factors, many cities have similar

60 topography, usually along the coasts, close to mountains or in basins. For these cities, the local
61 circulations induced by thermal contrast of the topography, such as sea-land breezes, mountain-
62 valley breezes and lake-land breezes, have an important impact on urban air quality under calm
63 conditions (Crosman and Horel, 2010). Examples can be found around the world. Ding et al. (2004)
64 simulated the main features of sea-land breezes during a multiday episode in the Pearl River Delta
65 (PRD) region, and found that the sea-land breezes can transport air pollutants between inland and
66 coastal cities. Miao et al. (2015) studied the effects of mountain-valley breezes on the boundary
67 layer structure in the Beijing-Tianjin-Hebei (BTH) region, suggesting that mountain-valley breezes
68 are vital to the vertical transport and distribution of air pollutants in Beijing. Wentworth et al. (2015)
69 identified a causal link between lake breezes and O₃ in the Greater Toronto Area that the daytime
70 O₃ maxima were 13.6-14.8 ppb higher on lake breeze days than on no-lake breeze days.

71 Ongoing urbanization, including changes in land use and anthropogenic heat (AH), can affect
72 meteorology and atmospheric compositions at local, regional and even global scales (Fu and Liao,
73 2014; Park et al., 2014; Oke et al., 2017). Land use changes via urban expansion (typically from
74 vegetation to impervious surface) directly alter the surface physical properties (e.g., albedo, surface
75 moisture and roughness), subsequently affecting the exchange of energy, moisture and momentum,
76 and hence impacting the urban climate and air quality (Jiang et al., 2008; Wang et al., 2009). Li et
77 al. (2019) found that increases in thermal inertia, surface roughness and evapotranspiration due to
78 urban expansion can rise O₃ by 5.6 ppb in Southern California. AH is an important waste by-product
79 of urban metabolism. Nearly all energy consumed by human activities will be dissipated as heat
80 within Earth's land-atmosphere system (Flanner, 2009; Sailor, 2011), which is then "injected" into
81 the energy balance processes. Ryu et al. (2013) reported that AH affects the characteristics/structures
82 of the boundary layer and local circulations, resulting in an increase in O₃ by 3.8 ppb in the Seoul
83 metropolitan area.

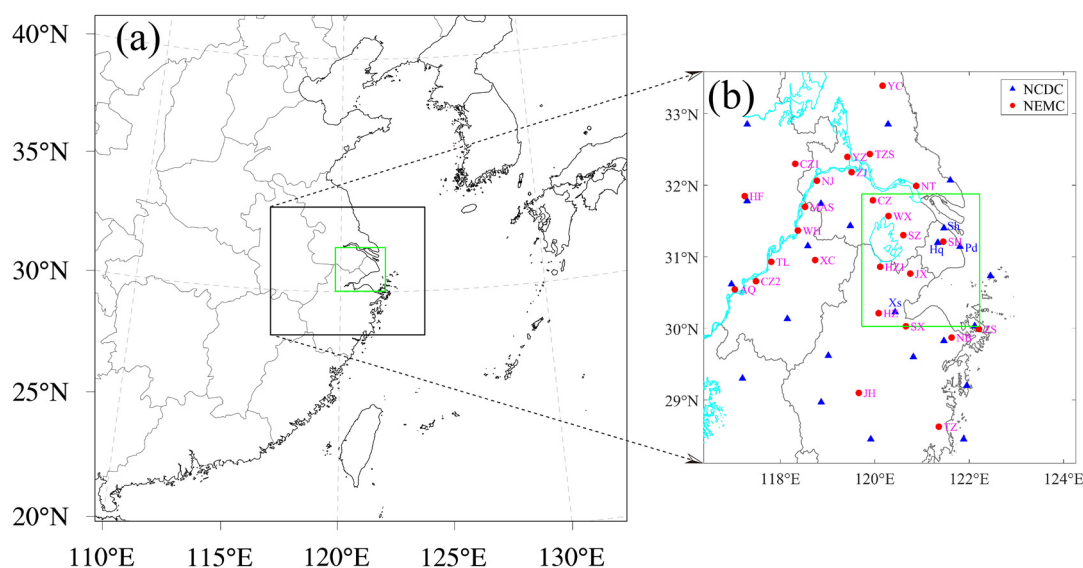
84 Previous studies usually investigated the impacts of topography, land use and AH on
85 meteorology and air quality separately, and mainly focused on a specific megacity. However, these
86 factors can work together in near-calm conditions. Furthermore, complex interactions exist widely
87 among thermally driven circulations, and the effects can even spread from one city to nearby areas.
88 For example, Zhu et al. (2015) demonstrated that the meteorological conditions and air quality over
89 Kunshan are significantly affected by Shanghai urban land surface forcing (Kunshan is located

90 downstream of Shanghai with a straight-line distance of approximately 50 km). Given the increasing
91 prevalence of cities, cities gradually appear in the form of clusters. Therefore, assessing the effects
92 of land use and AH (the topography rarely changes.) in city clusters is meaningful, which also helps
93 understand the interactions between the urban environment and human activities.

94 The Yangtze River Delta (YRD) region, located on the western coast of the Pacific Ocean
95 (Figure 1a), has undergone accelerated urbanization processes and rapid economic development
96 over the past few decades. It is now one of the largest economic zones in the world. The YRD region
97 consists of the southern part of Jiangsu Province, the northern part of Zhejiang Province and the
98 eastern part of Anhui Province, including 26 mega/large cities such as Shanghai, Hangzhou and
99 Nanjing (Figure 1b). With dense population and huge energy consumption, this area is now suffering
100 from air quality deterioration (Xie et al., 2017; Zhan et al., 2020), especially the increasingly severe
101 O₃ pollution in recent years (Li et al., 2020; Wang et al., 2020). Furthermore, cities with hot spots
102 of O₃ are usually concentrated in the central YRD region surrounding Tai Lake (Zhan et al., 2021).
103 Numerous cities, unique topography and severe O₃ pollution make the YRD an ideal study place.

104 In this study, the impacts of land use and AH on meteorology in the central YRD region, and
105 how these effects further modulate O₃ are investigated using the Weather Research and Forecasting
106 model coupled to Chemistry (WRF-Chem). These results fill the knowledge gap about the formation
107 of O₃ pollution in this region and provide valuable insight for other rapidly developing regions with
108 complex topography in the world. The remainder of this paper is organized as follows. Sect. 2 gives
109 a detailed description of the observation data, the model setup and the experimental design. The
110 main results, including the characteristics of O₃ pollution episodes, the model evaluation and the
111 changes in meteorology and O₃ caused by land use and AH, are presented in Sect. 3. Summary and
112 conclusions are given in Sect. 4.

113



114

115 **Figure 1.** (a) Three nested WRF-Chem domains. (b) The locations of cities (red dots) and weather
 116 stations (blue triangles) in the YRD. The green rectangular regions represent the innermost domain
 117 and also the central YRD region. The cities in (b) include: the megacity Shanghai (SH); Hangzhou
 118 (HZ), Ningbo (NB), Jiaxing (JX), Huzhou (HZ1), Shaoxing (SX), Jinhua (JH), Zhoushan (ZS) and
 119 Taizhou (TZ) located in Zhejiang Province; Nanjing (NJ), Wuxi (WX), Changzhou (CZ), Suzhou
 120 (SZ), Nantong (NT), Yancheng (YC), Yangzhou (YZ), Zhenjiang (ZJ) and Taizhoushi (TZS) located
 121 in Jiangsu Province; and Hefei (HF), Wuhu (WH), Maanshan (MAS), Tongling (TL), Anqing (AQ),
 122 Chuzhou (CZ1), Chizhou (CZ2) and Xuancheng (XC) located in Anhui Province.

123

124 **2 Materials and methods**

125 **2.1 Surface observations**

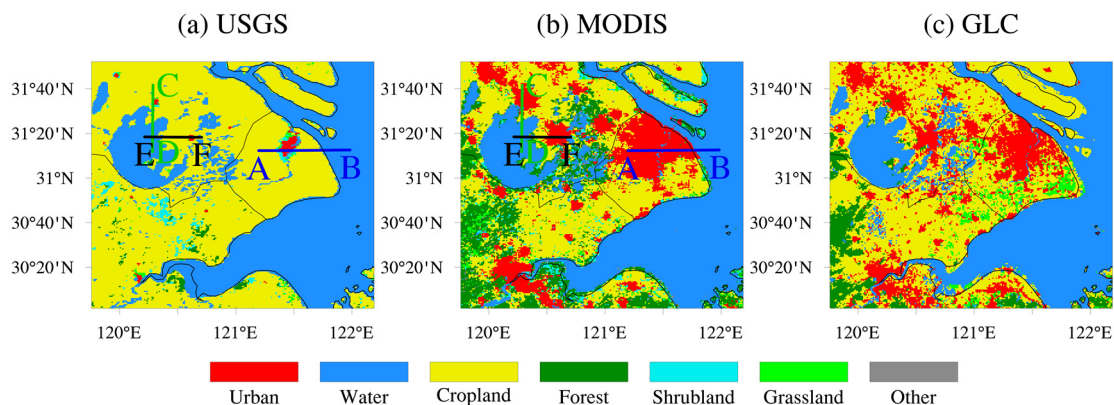
126 Hourly O₃ concentrations monitored by the National Environmental Monitoring Center
 127 (NEMC) of China are used in this study. These data strictly follow the national monitoring standards
 128 HJ 654-2013 and HJ 193-2013 (<http://www.cnemc.cn/jcgf/dqhj/>) and are available at
 129 <https://quotsoft.net/air/>. The nationwide observation network initially operated in 74 major cities
 130 since 2013, and it has grown to more than 1,500 stations covering 454 cities by 2017 (Lu et al.,
 131 2018). The urban hourly O₃ concentrations are the average results of measurements at all monitoring
 132 sites in that city. The daily maximum 8-h average (MDA8) O₃ concentrations are calculated using
 133 the hourly O₃ concentrations for days with more than 18-h measurements (Liao et al., 2017).

134 Meteorological data are taken from the National Climatic Data Center (NCDC), including 2-
 135 m air temperature (T_2), relative humidity (RH), 10-m wind speed (WS_{10}) and direction (WD_{10}) and
 136 cloud cover (CC). These data as well as the technical documents recording the quality control, data
 137 collection and archive are available at <ftp://ftp.ncdc.noaa.gov/pub/data/noaa/isd-lite/>. Locations of
 138 the weather stations are shown in Figure 1b. Specifically, the weather stations in the innermost
 139 domain are Pudong (Pd), Shanghai (Sh), Hongqiao (Hq) and Xiaoshan (Xs).

140 2.2 MODIS-based and USGS land use classifications

141 To explore the effects of land use, two land use categories defaulted in WRF are used to set up
 142 the first two scenario simulations (Table 2). The MODIS-based land cover product was created from
 143 500-m MODIS Terra and Aqua satellite imagery (Friedl et al., 2010) and replaced USGS as the
 144 default settings in WRF since version 3.8. The USGS data were primarily derived from the
 145 Advanced Very High Resolution Radiometer (AVHRR) from 1992 to 1993 at 1-km spatial
 146 resolution (Loveland et al., 2000), which reflects the distribution of cities in the late 1980s. Figure
 147 2 presents the land cover maps in the innermost domain. The most obvious difference between
 148 MODIS and USGS is the urban fraction, which is related to the urban expansion caused by rapid
 149 urbanization. In addition, the Finer Resolution Observation and Monitoring-Global Land Cover in
 150 2015 (GLC), one of the latest (2015) and finest (30-m) land cover datasets (Gong et al., 2019), is
 151 quite consistent with the performance of MODIS in this region. This confirms that the urban fraction
 152 in MODIS is close to reality. Thus, the MODIS data can generally refer to today's distribution of
 153 cities.

154



155

156 **Figure 2.** Land cover maps in the innermost domain, with (a) USGS, (b) MODIS, and (c) GLC

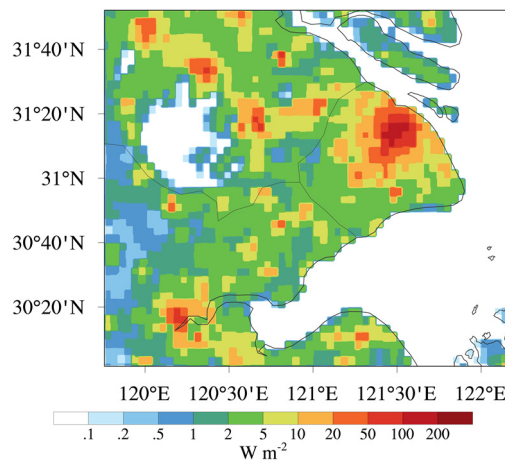
157 datasets.

158

159 **2.3 Anthropogenic heat flux modeling**

160 Another scenario simulation incorporates the urban canopy model with gridded AH fluxes to
161 diagnose the impact of AH. The AH fluxes were calculated based on the statistical data of energy
162 consumption of China in 2016, and then were gridded as 144 rows and 144 columns with a resolution
163 of 2.5° using population density downloaded from Columbia University's Socioeconomic Data and
164 Applications Center. AH fluxes with their diurnal variations are considered by adding them to the
165 sensible heat flux from the urban canopy layer within the Single Layer Urban Canopy Model
166 (SLUCM). The AH fluxes for each grid are determined by the fixed AH value for the urban land
167 use category, the urban fraction value on each grid and the fixed temporal diurnal pattern. Details
168 on the calculation of AH fluxes, and how to add AH fluxes into the model can be found in Xie et al.
169 (2016a, b). Figure 3 gives the spatial distribution of AH fluxes in the innermost domain. In urban
170 areas, the AH fluxes usually exceed 20 W m^{-2} . Some megacities, like Shanghai, can have an AH
171 flux value as high as 200 W m^{-2} . Except for the urban areas, the AH fluxes are generally less than 5
172 W m^{-2} in most parts of the YRD region. In particular, in places where there is no human activity, the
173 AH flux is 0.

174



175

176 **Figure 3.** Spatial distribution of anthropogenic heat fluxes in the innermost domain.

177

178 **2.4 Model setup and experimental designs**

179 In this study, WRF-Chem version 3.9.1 was applied. The WRF-Chem model is a fully coupled

180 online numerical weather prediction model with chemistry components (Grell et al., 2005), in which
 181 chemical and meteorological variables use the same coordinates, transport schemes and physics
 182 schemes in space and time. There are 32 vertical levels extending from the surface to 100 hPa with
 183 12 levels located below 2 km to resolve the boundary layer processes. The domain and options for
 184 physical and chemical parameterization schemes are summarized in Table 1. The initial and
 185 boundary conditions of meteorological fields are from the National Centers for Environmental
 186 Prediction (NCEP) global final analysis fields every 6 h at $1^\circ \times 1^\circ$ resolution. The anthropogenic
 187 emissions are provided by the Multiresolution Emission Inventory for China (MEIC) in 2017 with
 188 a resolution of 0.25° (<http://meicmodel.org/>), which includes 10 air pollutants and CO₂ from power,
 189 industry, residential, transportation and agriculture sectors. The biogenic emissions are calculated
 190 online using the Model of Emissions of Gases and Aerosols from Nature (MEGAN) available in
 191 WRF-Chem (Guenther et al., 2006). As our main objective is to explore the response of O₃ to the
 192 meteorological changes induced by land use and AH, we use the same surface biogenic emission
 193 rates for different land use scenarios (Li et al., 2014, 2017). Further studies will be carried out to
 194 quantify the contribution of biogenic volatile organic compounds changed by meteorological
 195 conditions to O₃.

196

197 **Table 1.** The domains and major options for WRF-Chem.

Items	Contents
Dimensions (x, y)	(101, 96), (146, 121), (236, 206)
Grid spacing (km)	25, 5, 1
Time step (s)	75
Microphysics	Purdue Lin microphysics scheme (Chen and Sun, 2002)
Longwave radiation	RRTM scheme (Mlawer et al., 1997)
Shortwave radiation	Goddard scheme (Kim and Wang, 2011)
Surface layer	Revised MM5 Monin-Obukhov scheme
Land-surface layer	Noah land-surface model (Chen and Dudhia, 2001)
Planetary boundary layer	YSU scheme (Hong et al., 2006)
Cumulus parameterization	Grell 3D ensemble scheme (Grell and Devenyi, 2002)

Gas-phase chemistry	RADM2 (Stockwell et al., 1990)
Photolysis scheme	Fast-J photolysis (Fast et al., 2006)
Aerosol module	MADE/SORGAM (Schell et al., 2001)

198

199 As shown in Table 2, three numerical experiments are performed. The MODIS_noAH
 200 experiment is a control simulation with commonly used settings. Compared with MODIS_noAH,
 201 USGS_noAH selects the USGS land use classification at runtime through the geogrid program.
 202 Thus, the difference between the modeling results of MODIS_noAH and USGS_noAH can illustrate
 203 the changes caused by land use. The impact of AH can be identified by comparing the modeling
 204 results of MODIS_AH and MODIS_noAH because AH is only added in MODIS_AH. To exclude
 205 the uncertainty conceivably caused by different configurations, all three simulations use the same
 206 emission inventory, physical and chemical parameterization schemes (Table 1), running from 00:00
 207 UTC 21 May to 00:00 UTC 4 June 2017 with the first 88 h as spin-up time.

208

209 **Table 2.** The three numerical experiments.

Scenario	Land use classification	Whether to add AH
MODIS_noAH	MODIS-based	No
USGS_noAH	USGS	No
MODIS_AH	MODIS-based	Yes

210

211 2.5 Model evaluation

212 To verify the model performance, the simulation results in the innermost domain, including O₃
 213 concentration, T₂, RH, WS₁₀ and WD₁₀ are examined against the surface observations described in
 214 Sect. 2.1. The statistical metrics, including the mean bias (MB), root mean square error (RMSE) and
 215 correlation coefficient (COR), are also calculated. They are defined as follows:

$$216 \quad MB = \frac{1}{N} \sum_{i=1}^N (S_i - O_i), \quad (1)$$

$$217 \quad RMSE = \sqrt{\frac{1}{N} \sum_{i=1}^N (S_i - O_i)^2}, \quad (2)$$

$$COR = \frac{\sum_{i=1}^N (S_i - \bar{S})(O_i - \bar{O})}{\sqrt{\sum_{i=1}^N (S_i - \bar{S})^2} \sqrt{\sum_{i=1}^N (O_i - \bar{O})^2}}, \quad (3)$$

where S_i and O_i are the simulations and observations, respectively. N is the total amount of valid data, and \bar{S} and \bar{O} represent the average of simulations and observations, respectively. Generally, the model performance is acceptable if the values of MB and $RMSE$ are close to 0, and that of COR is close to 1 (Xie et al., 2016a, b; Zhan et al., 2020).

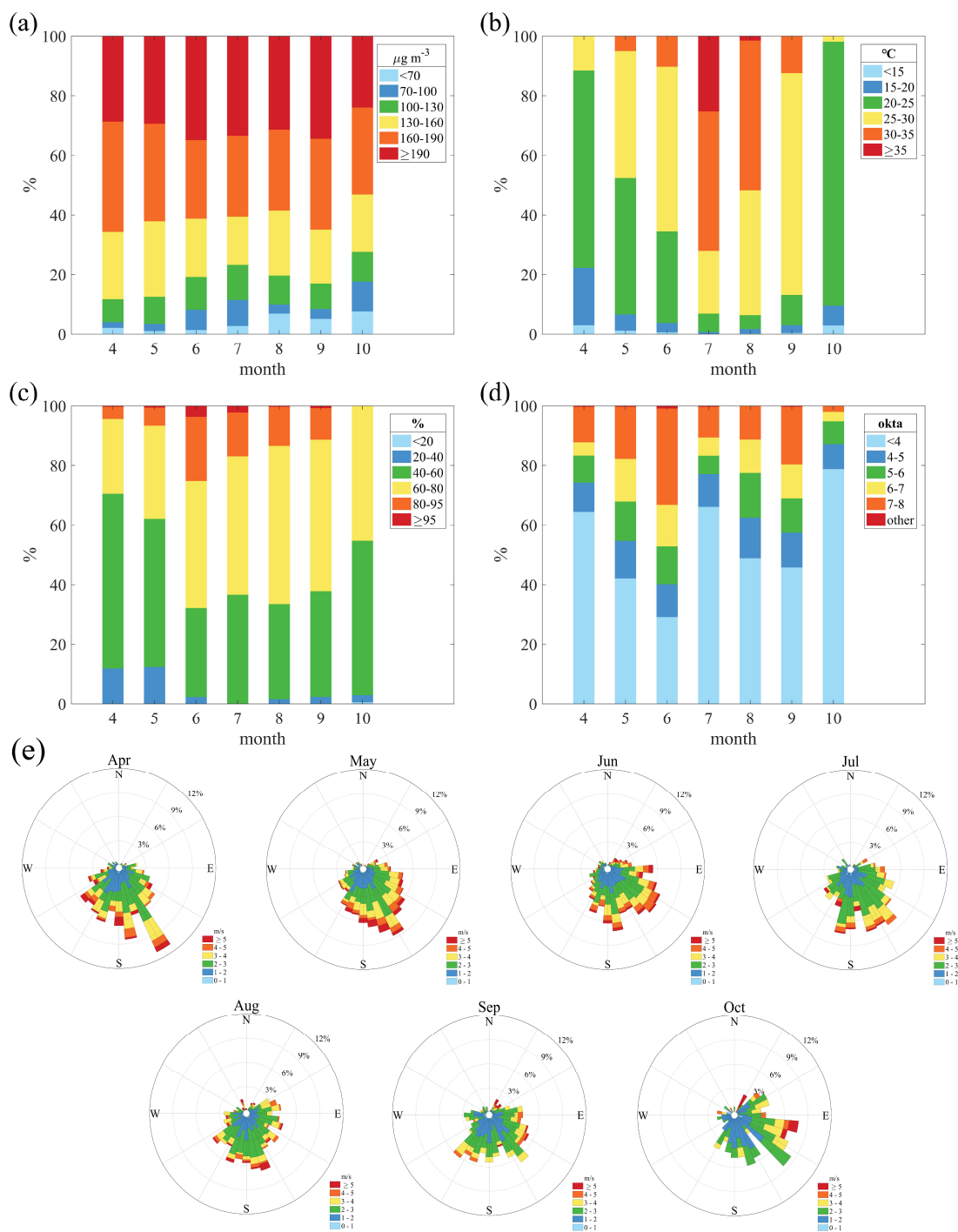
3 Results and discussions

3.1 Regional O₃ pollution episodes in the YRD

On cloudless sunny days, regional O₃ pollution episodes occur frequently in the YRD (Gao et al., 2020; Zhan et al., 2021), affecting an area of 3.5 million square kilometers and harming more than 200 million people. Regional O₃ pollution is generally defined as when more than half of the 26 typical cities in the YRD fail to meet the national O₃ standard (in China, the national ambient air quality standard for MDA8 O₃ is 160 μg m⁻³). Based on the surface O₃ observations, we sort out all regional O₃ pollution episodes and the corresponding weather patterns from 2015 to 2019 (Table S1). There were 20, 19, 34, 28 and 30 regional O₃ pollution cases in the YRD from 2015 to 2019, respectively. These cases mainly occurred in April to October of each year, and were usually related to high pressure, uniform pressure fields and typhoon activity.

Figure 4 further displays the monthly distribution of meteorological factors during the daytime (from 8:00 to 20:00 local time) when regional O₃ pollution occurs in the YRD. All the variables show significant monthly variations. The highest (lowest) temperature is found in July (April), and the relative humidity is highest in June. As for the cloud cover, the sky is covered with fewer clouds in October than in other months. In addition, southeast winds prevail in the YRD from April to October under the influence of the monsoon climate. The correlation coefficients between temperature, relative humidity, cloud cover, wind speed and MDA8 O₃ are 0.12, -0.34, -0.15 and 0.04, respectively. Therefore, O₃ pollution episodes tend to occur on days characterized by high temperature, low relative humidity, cloudless sky and light wind (the weak correlation between wind speed and MDA8 O₃ is due to the small change in light wind). More specifically, on days when the

245 temperature exceeds 20 °C (Figure 4b), the relative humidity is less than 80% (Figure 4c), the cloud
 246 cover is less than 5 okta (Figure 4d), and the wind speed is less than 3 m s⁻¹ (Figure 4e) in the YRD.
 247 On the other hand, local circulations are clearest when in absence of clouds, radiative heating is
 248 strongest and wind is weakest. In this case, local circulation will inevitably have an impact on the
 249 distribution of O₃.
 250



251

252 **Figure 4.** The monthly distributions of (a) MDA8 O₃, (b) temperature, (c) relative humidity, (d)
 253 cloud cover, and (e) wind speed and direction during the daytime (8:00 to 20:00 LT) when regional
 254 O₃ pollution occurs in the YRD.

255

256 **3.2 Case selection**

257 **3.2.1 Case for O₃ pollution episode**

258 For simplicity but without loss of generality, the longest-lasting regional O₃ pollution episode
 259 is selected to investigate the impacts of land use and AH on meteorology and O₃ in the YRD. This
 260 10-day regional O₃ pollution episode occurred from 25 May to 3 June 2017 (Table S1). Dominated
 261 by high pressure/uniform pressure fields (Figure S1), high O₃ concentrations are accompanied by
 262 high air temperature, low relative humidity, light wind and shallow cloud cover during this smog
 263 episode. An average of 18 out of the 26 cities experienced O₃ pollution every day with MDA8 O₃
 264 concentrations ranging from 80.0 to 269.0 $\mu\text{g m}^{-3}$ in the YRD. With regard to the meteorological
 265 factors, T₂ ranged from 12.9 to 33.5 °C, with an average of 26.4 °C; RH ranged from 26.6 to 99.4%,
 266 with an average of 58.6%; WS₁₀ ranged from 0.5 to 10.8 m s⁻¹, with an average of 2.8 m s⁻¹; CC
 267 ranged from 0 to 8.4 okta, with an average of 4.2 okta (Table 3). The values of these meteorological
 268 factors meet the standards in the previous section and can cover both the whole YRD and the central
 269 YRD region (the innermost domain). Therefore, this O₃ pollution episode not only meets the
 270 requirements of high O₃ concentrations but also calm weather conditions. The long duration also
 271 provides relatively universal results.

272

273 **Table 3.** Mean, minimum and maximum of MDA8 O₃, T₂, RH, WS₁₀ and CC during the daytime
 274 from 25 May to 3 June 2017.

	The YRD region			The central YRD region		
	Mean	Minimum	Maximum	Mean	Minimum	Maximum
MDA8 O ₃ ($\mu\text{g m}^{-3}$)	182.1	80.0	269.0	177.8	118.0	251.0
T ₂ (°C)	26.4	12.9	33.5	26.7	21.4	29.8
RH (%)	58.6	26.6	99.4	52.9	33.8	73.7
WS ₁₀ (m s ⁻¹)	2.8	0.5	10.8	3.6	1.6	6.0
CC (okta)	4.2	0	8.4	3.3	0	7.4

275

276 **3.2.2 Evaluation of model performance**

277 To evaluate the model performance, the simulation results in the innermost domain are
278 validated by comparing with the observational data. Table 4 presents the statistical metrics in
279 meteorological factors. Figure 5 further illustrates the time series of these meteorological factors
280 and their modeling results. T_2 is reasonably well simulated as the CORs (the mean of all the sites)
281 are 0.87, 0.86 and 0.86 in MODIS_noAH, USGS_noAH and MODIS_AH, respectively. The small
282 negative MBs at all sites suggest that our simulations underestimate T_2 to some extent, although this
283 light underestimation is acceptable because of the small RMSEs (2.3, 3.1 and 2.3 °C). The MBs for
284 T_2 in USGS_noAH, MODIS_noAH and MODIS_AH are -2.4, -1.0, and -0.8 °C. The smaller
285 RMSEs and MBs indicate that the T_2 simulation is improved when new land use and AH are taken
286 into account, which may be related to the improved latent and sensible heat fluxes in models (De
287 Meij and Vinuesa, 2014). The improvement can also be confirmed by Figure 5a. With respect to RH,
288 the CORs are 0.82, 0.75 and 0.83 in MODIS_noAH, USGS_noAH and MODIS_AH, respectively.
289 Thus, all three simulations can capture the diurnal variation of RH well but have different
290 performances at different sites. In USGS_noAH, RH is overestimated at all sites, especially the
291 Pudong site with an MB of 11.2%. While RH is overestimated at the two coastal sites (Pudong and
292 Shanghai) but underestimated at other two sites (Hongqiao and Xiaoshan) in MODIS_noAH and
293 MODIS_AH. Moreover, USGS_noAH has the highest RMSEs of RH (16.3%), followed by
294 MODIS_AH (12.4%) and MODIS_noAH (12.1%). Among the three experiments, the simulation
295 result of RH in USGS_noAH is the worst (Figure 5b). As for WS_{10} , the modeling values are slightly
296 overestimated at all sites in all three simulations. The overestimation of WS_{10} may partly be
297 attributed to the unresolved terrain features by the default surface drag parameterization causing an
298 overestimation of wind speed especially at low values (Jimenez and Dudhia, 2012). In particular,
299 WS_{10} in USGS_noAH is the most overestimated, followed by MODIS_AH and MODIS_noAH with
300 MBs of 1.2, 1.0 and 0.8 $m s^{-1}$, respectively. In addition, high MBs of WS_{10} correspond to high
301 RMSEs (1.9, 1.8 and 1.7 $m s^{-1}$) in our simulations. The MODIS-based land cover shows a larger
302 urban fraction, and thereby leads to more friction and higher roughness than the USGS dataset. In
303 this case, the overestimation of WS_{10} is somewhat neutralized to fit the observations. In terms of
304 WD_{10} , the model captures well the shift in wind direction during the study period (Figure 5d). In
305 summary, both the statistical metrics in Table 4 and the time series in Figure 5 indicate that all three
306 numerical experiments can capture the major changes in meteorological factors during this O_3

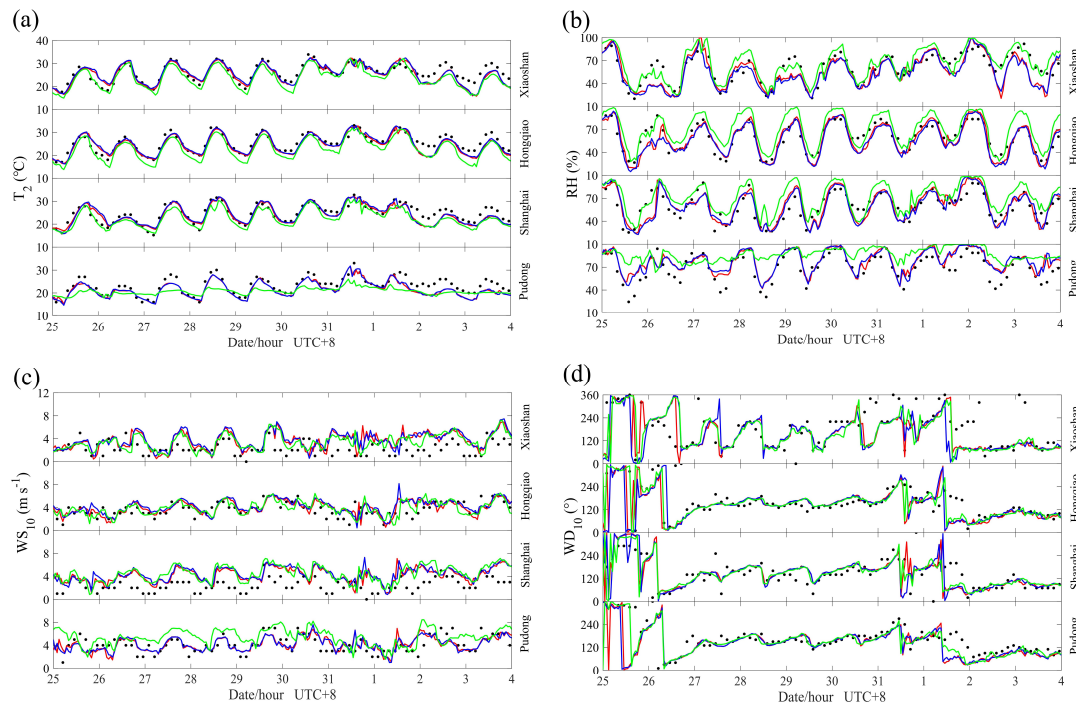
307 pollution episode. Nevertheless, updating the land use and adding AH can reduce the
308 underestimation of T_2 and the overestimation of RH and WS_{10} in models. Benefitting from the
309 development of computers, numerical models grow more complex, and the resolution requirements
310 are higher. This puts forward demands on many basic parameters. An updated land cover dataset,
311 like the GLC, contains useful information and can improve the model results (Chen et al., 2016;
312 Wang et al., 2018). Some factors that are generally ignored in models, like the AH fluxes, should
313 also be estimated and evaluated.

Table 4. Statistical metrics in meteorological variables between observations and simulations.

Variables	Site	MODIS_noAH				USGS_noAH				MODIS_AH				
		\bar{O}^a	\bar{S}^b	MB ^c	RMSE ^d	COR ^e	\bar{S}	MB	RMSE	COR	\bar{S}	MB	RMSE	COR
T ₂ (°C)	Pd	23.2	21.5	-1.7	2.4	0.89	20.7	-2.5	3.8	0.70	21.5	-1.7	2.4	0.89
	Sh	24.6	23.9	-0.7	2.2	0.87	22.5	-2.1	2.7	0.90	24.2	-0.5	2.3	0.84
	Hq	25.3	24.4	-0.9	2.0	0.89	22.7	-2.6	3.0	0.95	24.8	-0.5	1.9	0.89
	Xs	25.9	25.1	-0.8	2.4	0.85	23.8	-2.2	2.8	0.91	25.5	-0.4	2.4	0.83
RH (%)	Pd	69.1	77.7	8.6	13.5	0.81	86.2	17.2	23.4	0.45	77.7	8.7	13.3	0.83
	Sh	59.3	60.6	1.3	11.7	0.81	71.1	11.8	16.1	0.81	59.4	0.1	12.4	0.78
	Hq	59.5	57.7	-1.8	9.8	0.88	70.6	11.1	14.5	0.89	56.2	-3.3	9.8	0.89
	Xs	60.6	55.4	-5.2	13.5	0.79	65.3	4.8	11.3	0.86	53.5	-7.1	14.1	0.80
WS ₁₀ (m s ⁻¹)	Pd	4.1	4.1	0.0	1.4	0.47	5.5	1.3	2.1	0.35	4.2	0.1	1.3	0.51
	Sh	2.5	4.2	1.7	2.2	0.36	4.5	2.0	2.4	0.54	4.3	1.9	2.3	0.35
	Hq	3.7	3.9	0.2	1.2	0.54	3.9	0.2	1.2	0.53	4.2	0.5	1.3	0.50
	Xs	2.3	3.6	1.3	2.0	0.26	3.4	1.1	1.8	0.30	3.8	1.5	2.1	0.24
WD ₁₀ (°)	Pd	160.4	136.1	-26.2	78.7	0.42	148.1	-14.3	55.1	0.72	137.3	-24.7	77.5	0.42
	Sh	141.6	146.4	4.8	66.4	0.60	141.7	0.1	63.9	0.59	142.6	1.0	69.9	0.56
	Hq	159.7	140.2	-23.4	80.2	0.46	153.1	-10.6	74.9	0.52	142.8	-20.4	91.8	0.29
	Xs	188.6	160.2	-28.4	99.5	0.48	161.4	-27.3	109.6	0.35	152.0	-36.6	109.9	0.38

315 ^a \bar{O} and ^b \bar{S} indicate the average of observations and simulations, respectively. ^c MB indicates the mean bias, ^d RMSE indicates the root mean square error and ^e COR

316 indicates the correlation coefficient, with statistical significance at the 99% confidence level.



318

319 **Figure 5.** Time series of (a) T_2 , (b) RH, (c) WS_{10} and (d) WD_{10} for observations and simulations at
 320 different weather stations. The black dots are the surface observations. The simulation results of
 321 MODIS_noAH, USGS_noAH and MODIS_AH are shown in red, green and blue lines, respectively.

322

323 Table 5 lists the statistical metrics in O_3 , and Figure 6 gives the hourly variations in O_3 for
 324 observations and simulations in different cities. With high CORs (the CORs are 0.80, 0.81 and 0.80
 325 in MODIS_noAH, USGS_noAH and MODIS_AH, respectively), all three simulations well
 326 reproduce the diurnal variation in O_3 , which is that O_3 concentration reaches its maximum in the
 327 afternoon and decreases to its minimum in the morning. The magnitudes of O_3 modeling results are
 328 reasonable (Figure 6), but the peak and valley values of O_3 simulations sometimes differ from the
 329 observations, especially the peak values, like Huzhou. Considering the relatively low MBs (6.9, -
 330 1.6 and $9.0 \mu\text{g m}^{-3}$) and RMSEs (49.3 , 46.2 and $49.0 \mu\text{g m}^{-3}$), the modeling results of O_3 are generally
 331 reasonable and acceptable.

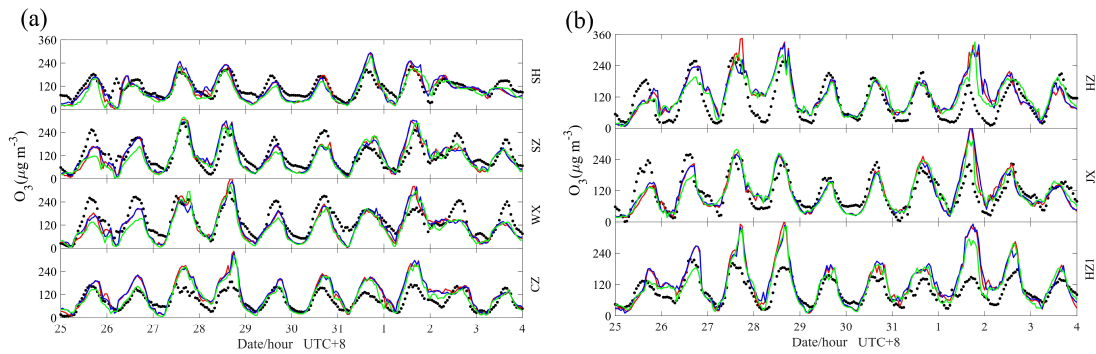
332

333 **Table 5.** Statistical metrics in O_3 ($\mu\text{g m}^{-3}$) between observations and simulations.

Case	Index	City						
		CZ	WX	SZ	SH	HZ1	JX	HZ

	\bar{O}	89.7	141.8	121.7	112.8	95.8	113.2	104.8
MODIS_noAH	\bar{S}	123.2	117.6	116.2	103.4	128.1	112.5	127.5
	MB	33.3	-24.2	-5.6	-9.1	32.1	-0.6	22.7
	RMSE	53.8	49.1	42.8	36.4	59.9	44.4	58.6
	COR	0.85	0.83	0.82	0.80	0.83	0.78	0.71
USGS_noAH	\bar{S}	108.1	106.8	107.1	93.8	118.6	111.0	122.5
	MB	18.5	-35.0	-14.7	-18.9	23.0	-2.0	18.0
	RMSE	43.5	56.0	44.7	37.7	50.1	41.1	50.0
	COR	0.83	0.81	0.80	0.81	0.82	0.80	0.77
MODIS_AH	\bar{S}	124.5	119.8	119.1	108.0	130.3	113.7	127.8
	MB	34.7	-21.9	-2.7	-4.6	34.3	0.6	23.0
	RMSE	53.5	47.3	42.4	37.4	59.4	44.7	58.2
	COR	0.84	0.83	0.81	0.80	0.82	0.78	0.71

334



335

336 **Figure 6.** Same as Figure 5, but for O₃.

337

338 Above all, the WRF-Chem model using our configuration has a good capability in simulating
 339 the meteorological factors and O₃ over the studied region. In addition, it is noteworthy that the object
 340 of inter-comparisons between the three numerical experiments are not to determine which setting is
 341 the most skillful in reproducing the observations. Rather, it is to diagnose and understand the
 342 changes induced by land use and AH, and the response of O₃ to these changes.

343

344 3.3 Overall behaviors of O₃ and local circulations

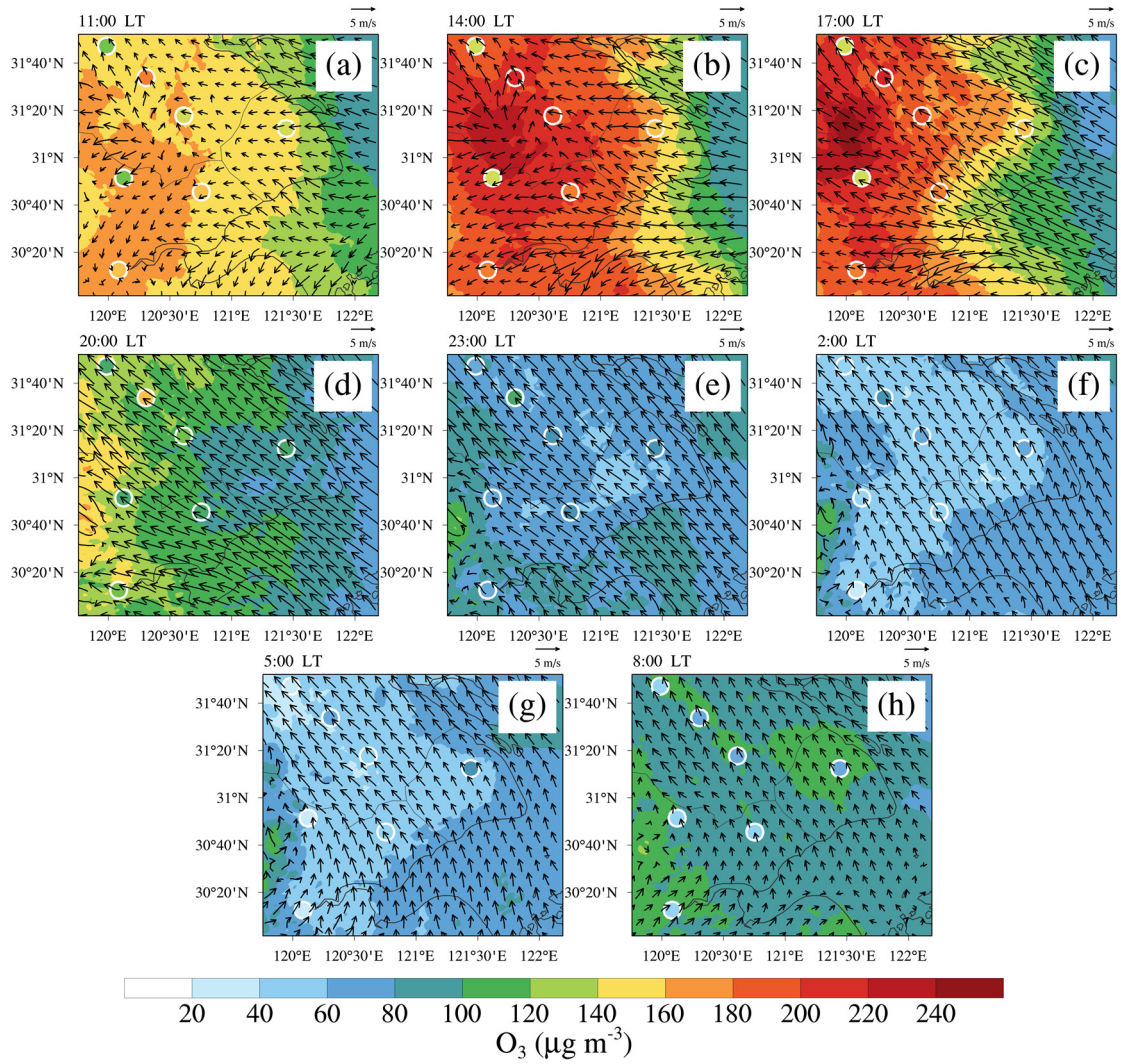
345 Based on the results of the control simulation (MODIS_noAH), we first give an overall
 346 behavior of O₃ and local circulations during the study period. Then the changes induced by land use
 347 and AH are discussed via inter-comparisons between different numerical experiments. Therefore,
 348 only difference plots between USGS_noAH/MODIS_AH and MODIS_noAH are shown in this
 349 paper, and the corresponding original plots for USGS_noAH/MODIS_AH can be found in the

350 supplementary materials (Figure S2-7).

351 **3.3.1 Spatiotemporal variations of O₃**

352 As shown in Figure 7, O₃ concentration began to rise around 8:00 local time (LT = UTC + 8 h)
353 and became noticeable after only 3 hours (Figure 7a and h). During this stage, the nocturnal residual
354 layer vanished due to the development of the convective boundary layer (Figure 8). The O₃-rich air
355 mass in the residual layer was mixed with the O₃-poor air mass on the ground, which enhanced the
356 surface O₃ in the morning (Hu et al., 2018). Around 11:00 LT, a convective boundary layer was
357 established (Figure 8), and high O₃ produced by photochemical reactions appeared over the central
358 YRD and persisted until 18:00 LT (Figure 7b and c). After sunset, surface O₃ concentration generally
359 decreased due to nitrogen oxide (NO) titration, and reached its minimum in the early morning
360 (Figure 7f and g). In general, O₃ has a typical diurnal variation with high concentrations in the
361 daytime and low concentrations at night. This is consistent with the observations in Figure 6, and
362 this rule of O₃ can be applied to most parts of the world. Therefore, the situation during the daytime
363 (we select 11:00, 14:00, 17:00 and 20:00 LT in this study) should be considered in regard to O₃
364 pollution.

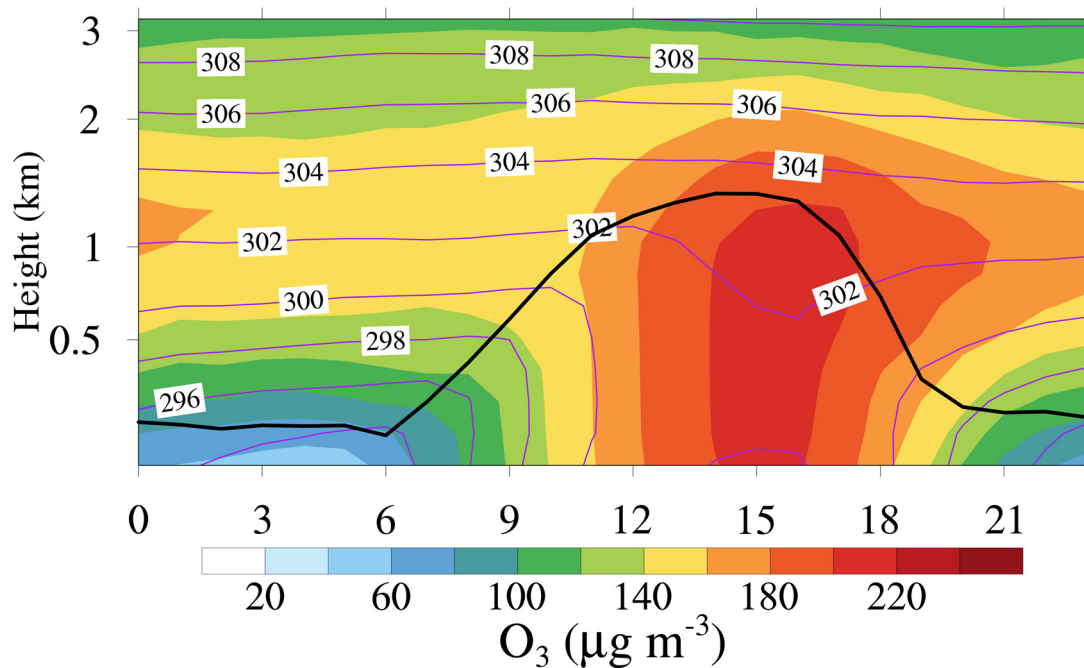
365



366

367 **Figure 7.** Horizontal distributions of O_3 and wind at the lowest model level in MODIS_noAH. (a),
 368 (b), (c) and (d) show the results at 11:00, 14:00, 17:00 and 20:00 LT, referring to the daytime. (e),
 369 (f), (g) and (h) show the results at 23:00, 2:00, 5:00 and 8:00 LT, referring to the night. The
 370 observations in different cities are overlaid using colored circles. To obtain universal features, all
 371 results are the average of the study period, and the same for the subsequent results.

372



373

374 **Figure 8.** Temporal-vertical distribution of O₃ and potential temperature covering the CZ, WX, SZ,
 375 SH, HZ1, JX and HZ over the innermost domain in MODIS_noAH.

376

377 3.3.2 The sea and lake breezes

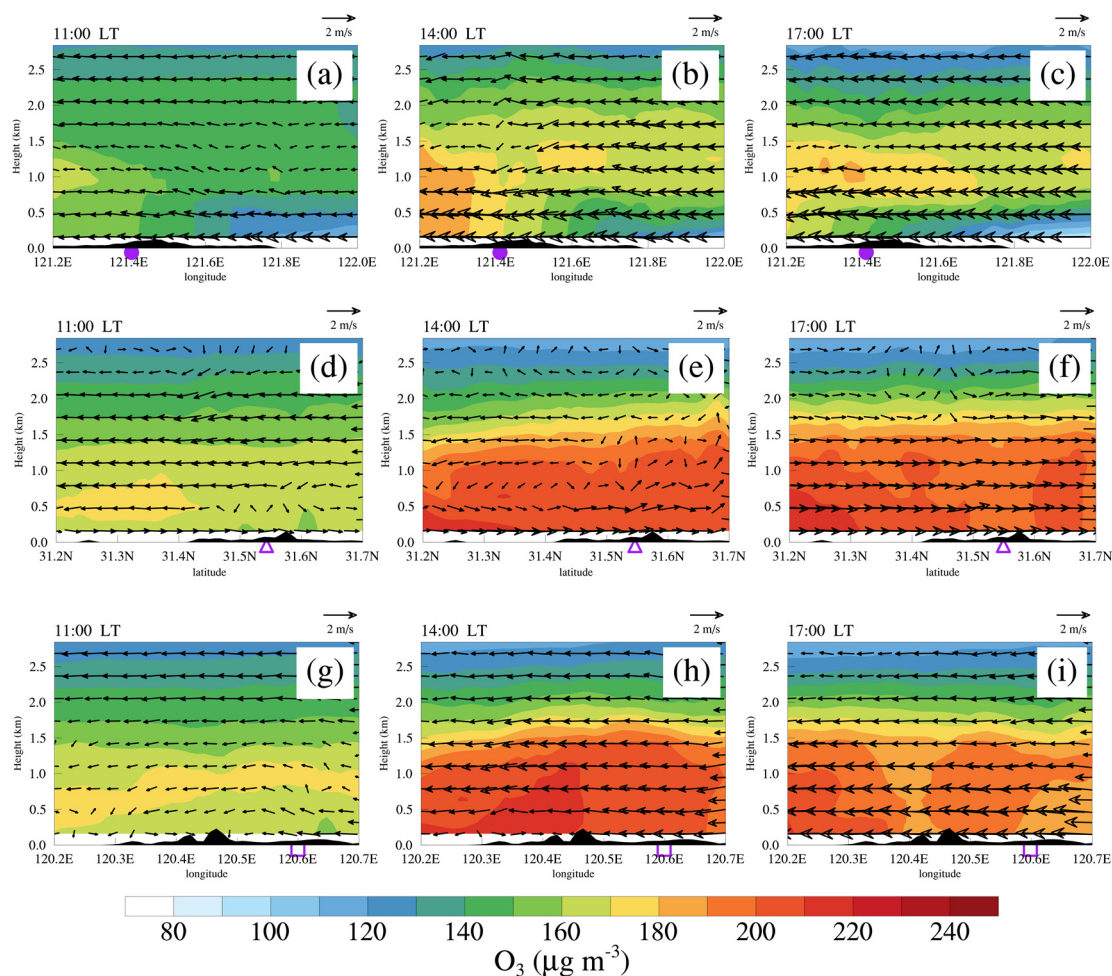
378 As shown in Figure 7a and b, high O₃ concentrations in the central YRD tended to appear in
 379 the converging airflows associated with the sea breeze, the lake breeze and the background southeast
 380 wind (Figure 4e). The sea breeze and the background southeast wind were usually in the same
 381 direction, and thereby sea breeze affected a wide area and lasted a long time. The sea breeze was
 382 obvious around 14:00 LT, matured around 17:00 LT, and continuously transported high O₃ from
 383 coastal to inland areas during this period (Figure 7b-d). Compared with the sea breeze, the lake
 384 breeze had a much smaller influencing area and a shorter duration. Around 11:00 LT, the lake breeze
 385 was established. It reached its maximum intensity around 14:00 LT and then disappeared sharply
 386 due to the predominant southeast wind (Figure 7b and c). Both the sea and the lake breezes are the
 387 typical local circulations in the YRD, and play important roles in the horizontal distributions of O₃
 388 over this region.

389 Since the coastline is generally north-south (Figure 1b), the cross sections along blue line AB
 390 (east-west) depicted in Figure 2a are illustrated to show representative examples of the vertical
 391 structure of the sea breeze (Figure 9a-c). By 11:00 LT, the sea breeze below 500 m had already

392 developed. The sea breeze front was found in front of Shanghai ($\sim 121.6^\circ\text{E}$), with a height of 1.5 km
393 (Figure 9a). Around 14:00 LT, the speed of sea breeze increased, exceeding 5 m s^{-1} . The sea breeze
394 front moved inland for a distance of 20-30 km ($\sim 121.4^\circ\text{E}$), and was elevated to $\sim 2 \text{ km}$ (Figure 9b).
395 Around 17:00 LT, the sea breeze matured, reducing the O_3 concentration near the surface in
396 Shanghai. However, the O_3 in the mixed layer still maintained a high level, which may result in an
397 O_3 -rich reservoir forming in the nocturnal residual layer (Figure 9c). The penetration of the sea
398 breeze front and its effect on surface O_3 are also observed in other coastal regions, such as Taiwan
399 (Lin et al., 2007), the Athens basin (Mavrakou et al., 2012) and Paulo (Freitas et al., 2007).

400 As for the lake breeze, since the lake is inside the land, the lake breeze has different directions.
401 Thus, the cross sections along green line CD (south-north) and black line EF (east-west) in Figure
402 2a are given. The lake breeze was established by 11:00 LT (Figure 9d and g) although it was shallow
403 at that time. Around 14:00 LT, the lake breeze strengthened. The extension of the lake breeze
404 circulation zone can reach up to 2 km in the vertical dimension (Figure 9e). The offshore flow of
405 the lake breeze circulation ($\sim 2 \text{ m s}^{-1}$) transported high O_3 concentrations from the urban areas to the
406 lake, while the onshore flow blew the O_3 back to urban areas (Figure 9e and h). Thus, the net effect
407 of the lake breeze is to accelerate the vertical mixing of O_3 in the boundary layer, resulting in high
408 surface O_3 in the lakeside cities. This was also reported in other lakeside cities, such as the Lake
409 Michigan (Lennartson and Schwartz, 2002), the Great Lakes (Sills et al., 2011) and the Great Salt
410 Lake (Blaylock et al., 2017). By 17:00 LT, the lake breeze disappeared.

411



412

413 **Figure 9.** Vertical cross sections of O_3 and wind for the sea breeze at (a) 11:00, (b) 14:00 and (c)
 414 17:00 LT along blue line AB in Figure 2a. (d), (e) and (f) are the same as (a), (b) and (c), respectively,
 415 but for the lake breeze along green line CD in Figure 2a. (g), (h) and (i) are also the same as (a), (b)
 416 and (c), respectively, but for the lake breeze along black line EF in Figure 2a. The purple dots,
 417 triangles and rectangles represent the locations of Shanghai, Wuxi and Suzhou, respectively. The
 418 black shaded areas represent the terrain, and the terrain is multiplied by a factor of 10 when plotting.

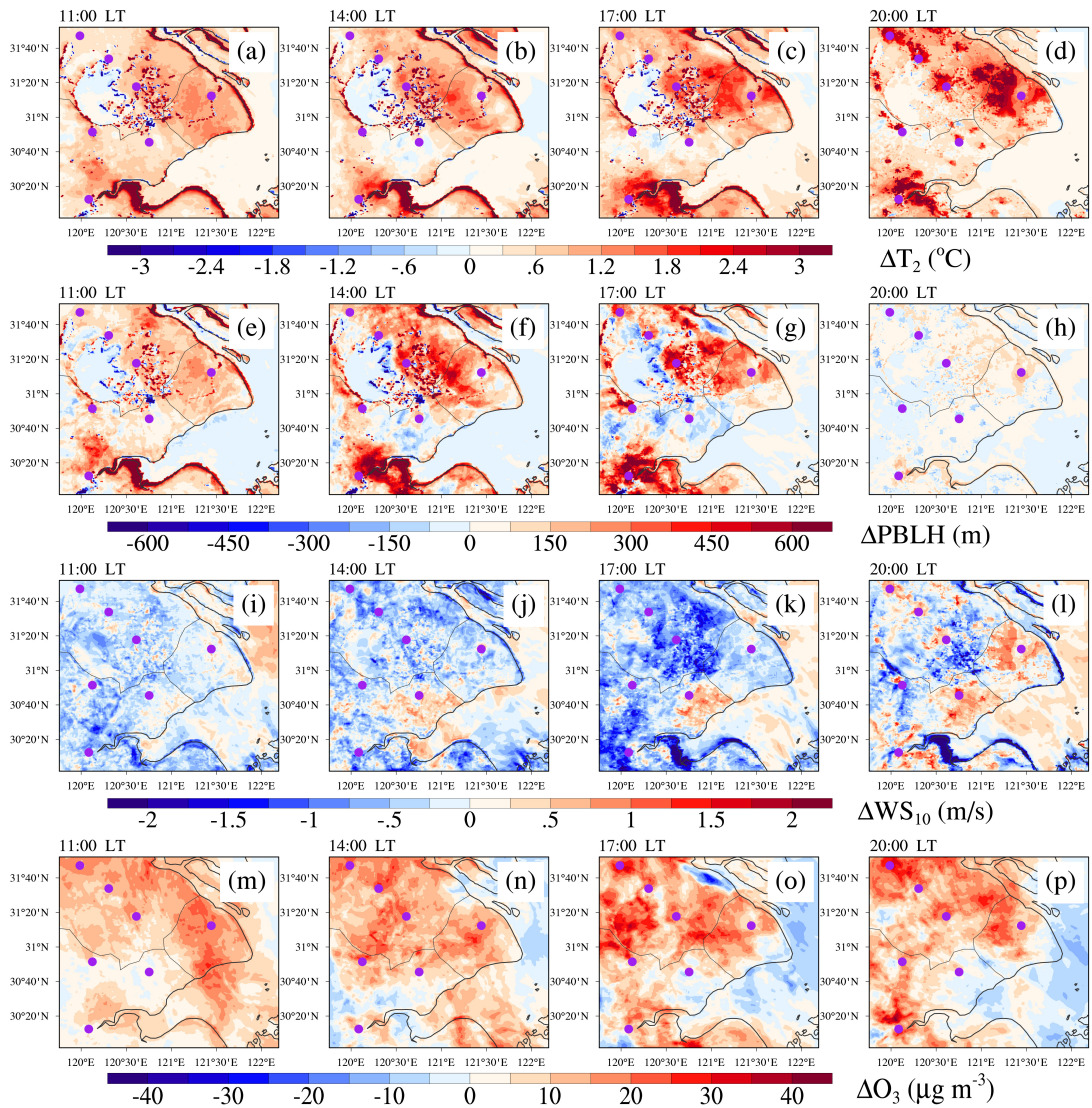
419

420 3.4 Impacts of land use on meteorology and O_3

421 3.4.1 The changes in horizontal direction

422 Figure 10 presents the spatial differences of the main factors (T_2 , PBLH, WS_{10} and O_3) between
 423 MODIS_noAH and USGS_noAH. Land use changes via urban expansion can enhance surface
 424 heating through upward sensible heat fluxes so that T_2 will increase. As shown in Figure 10a-d, the
 425 spatial pattern of the remarkable warming effect for T_2 was consistent with the urban fraction change

426 associated with urbanization (Figure 2a and b), which is the positive temperature anomaly that
427 mainly appeared in cities and their surrounding areas. In megacities like Shanghai, T_2 increased by
428 even 3 °C. The change in PBLH was similar to that in T_2 because the warming up of T_2 was
429 conducive to vertical movement in the boundary layer, which increased the PBLH (Figure 10e-h).
430 The maximum positive change of PBLH can reach up to 500 m at noon but down to 100 m after
431 sunset. With regard to WS_{10} , it decreased in MODIS_noAH (Figure 10i-l), with a maximum
432 decrease up to 1.5 m s⁻¹ in Hangzhou around 17:00 LT. This is because the roughness of cities and
433 forest is larger than that of cropland (Figure 2a and b). Apart from the abovementioned
434 meteorological factors, urban expansion also increased the surface O₃ concentration (Figure 10m-
435 p). The largest increment of O₃ appeared in the afternoon, with a value of 20 µg m⁻³ around 17:00
436 LT in Changzhou. In addition to these results, it is noteworthy that there were confusing “false”
437 changes at the junction of land and sea/lake, especially for meteorological factors, such as T_2 and
438 WS_{10} . This was caused by the different treatments of the MODIS-based and USGS land use
439 classifications at the boundary conditions of land versus water instead of urban expansion.
440



441
 442 **Figure 10.** Horizontal distributions of the differences of (a-d) T_2 , (e-h) PBLH, (i-l) WS_{10} and (m-p)
 443 O_3 between MODIS_noAH and USGS_noAH (MODIS_noAH – USGS_noAH) during the daytime.
 444 The purple dots represent the locations of cities in the innermost domain.

445

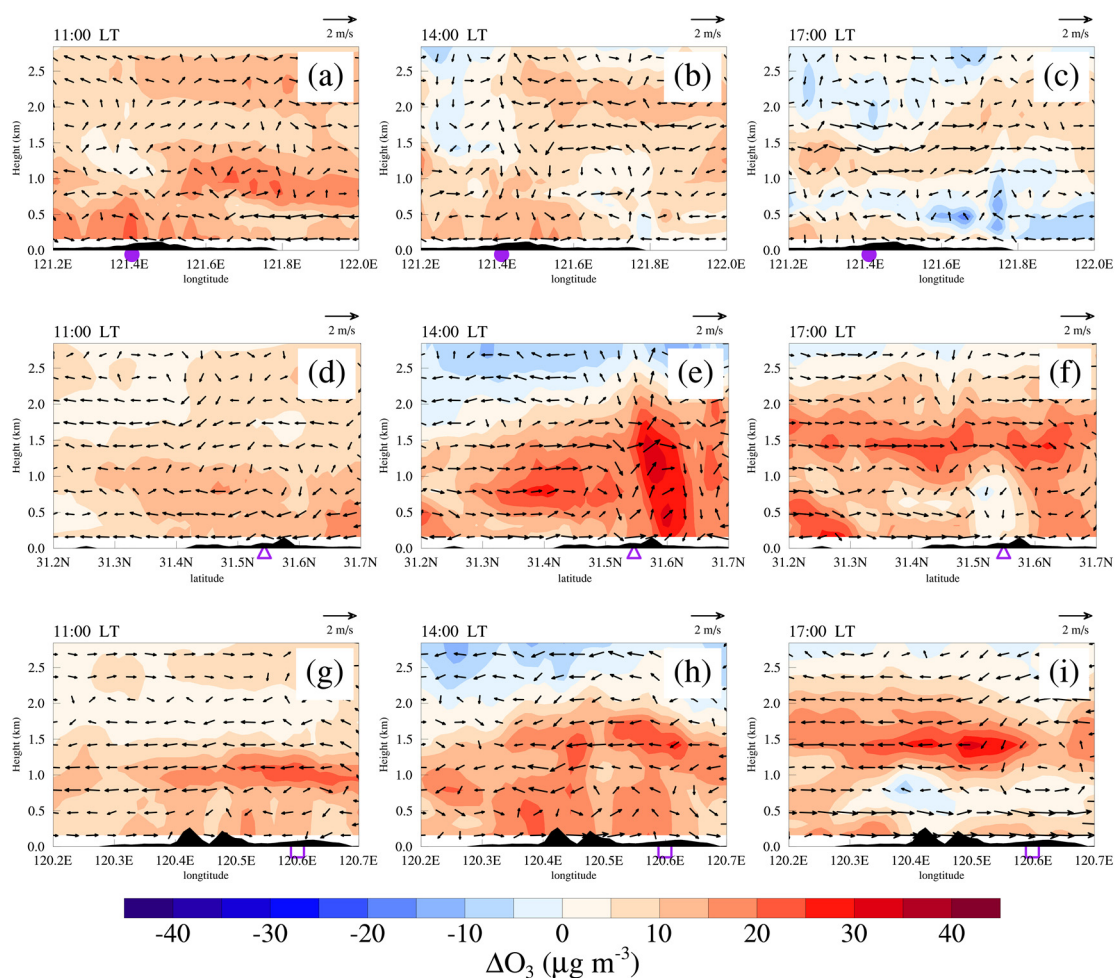
446 3.4.2 The changes in vertical direction

447 Urban expansion alters not only the meteorological factors but also the local circulations. As
 448 shown in Figure 11a-c, the sea breeze below 500 m increased by $\sim 1 \text{ m s}^{-1}$ due to the enhanced
 449 temperature contrast between the land and the sea induced by the expansion of Shanghai. During
 450 the advance of the sea breeze front inland, the updraft induced by the sea breeze front promoted the
 451 vertical mixing of O_3 , elevating the surface O_3 concentration in Shanghai (Figure 11a and b). When
 452 the sea breeze matured around 17:00 LT, its transport effect reduced the surface O_3 concentration of
 453 the coastal cities (Figure 9c). However, this “transport effect” was weakened because the sea breeze

454 near the surface was slowed affected by the rough urban surface. Finally, surface O_3 of $\sim 10 \mu g m^{-3}$
 455 was left compared to the scenario without cities. In contrast to the onshore flow, the offshore flow
 456 transported O_3 to the sea, which may be an important source of O_3 in the nocturnal residual layer.
 457 Influenced by the strong background southeast wind, the offshore flow was imperceptible during
 458 the daytime (Figure 9), but it was enhanced by urban expansion (Figure 11c).

459 As for the lake breeze, it was also enhanced by $\sim 1 m s^{-1}$ because of the larger temperature
 460 contrast resulting from the expansion of lakeside cities (Figure 11e and h). Moreover, the life of the
 461 lake breeze was extended to 17:00 LT (Figure 11f and i). Since the lake breeze circulation was
 462 conducive to the vertical mixing of O_3 in the boundary layer (Sect. 3.3.2), the O_3 concentration will
 463 increase in the lakeside cities, with a maximum of $30 \mu g m^{-3}$ in Wuxi at 14:00 LT.

464



465

466 **Figure 11.** Same as Figure 9, but for the differences between MODIS_noAH and USGS_noAH
 467 (MODIS_noAH – USGS_noAH).

468

469 **3.4.3 The mechanism of land use modulating O₃**

470 Changing land use from USGS to MODIS leads to an increase in T₂ by a maximum of 3 °C,
471 an increase in PBLH by a maximum of 500 m and a decrease in WS₁₀ by a maximum of 1.5 m s⁻¹
472 in the YRD, which is comparable to those in the BTH region (Yu et al., 2012), the PRD region (Li
473 et al., 2014) and the National Capital Region of India (Sati and Mohan, 2017). These changes are
474 particularly evident in and around cities as the largest change in land use is urban surface fractions.
475 Elevated air temperature is conducive to the photochemical production of O₃, and the well-
476 developed convective boundary layer favors the vertical mixing of O₃. These changes in
477 meteorological factors eventually increase the surface O₃ concentration by a maximum of 20 μg m⁻³
478 in the YRD. Furthermore, local circulations, including the sea and the lake breezes, are also
479 influenced by urban expansion, which further alters O₃ in the vertical direction. For coastal cities,
480 like Shanghai, the larger temperature contrast caused by cities enhances the sea breeze. As the sea
481 breeze front moves inland, it enhances upward movement, which is conducive to the mixing of O₃
482 in the boundary layer. However, the movement of the sea breeze is slowed due to the rough urban
483 surface after the sea breeze matures. The removal of O₃ via the sea breeze near the surface is then
484 weakened. A similar response of the sea breeze to cities as well as its impact on O₃ has also been
485 reported in the PRD region (You et al., 2019) and Paulo (Freitas et al., 2007). For the lakeside cities,
486 like Wuxi and Suzhou, the lifetime of lake breezes is extended to the afternoon due to the expansion
487 of cities. The offshore flow of the lake breeze transports high O₃ concentrations in the middle of the
488 boundary layer from the land to the lake, while the onshore flow brings the O₃ back to the land,
489 which accelerates the vertical mixing of O₃ and increases the surface O₃. Thus, high surface O₃
490 usually appears when the lake breeze is established. This was also observed in the Greater Toronto
491 Area (Wentworth et al., 2015) and the Lake Michigan (Abdi-Oskouei et al., 2020).

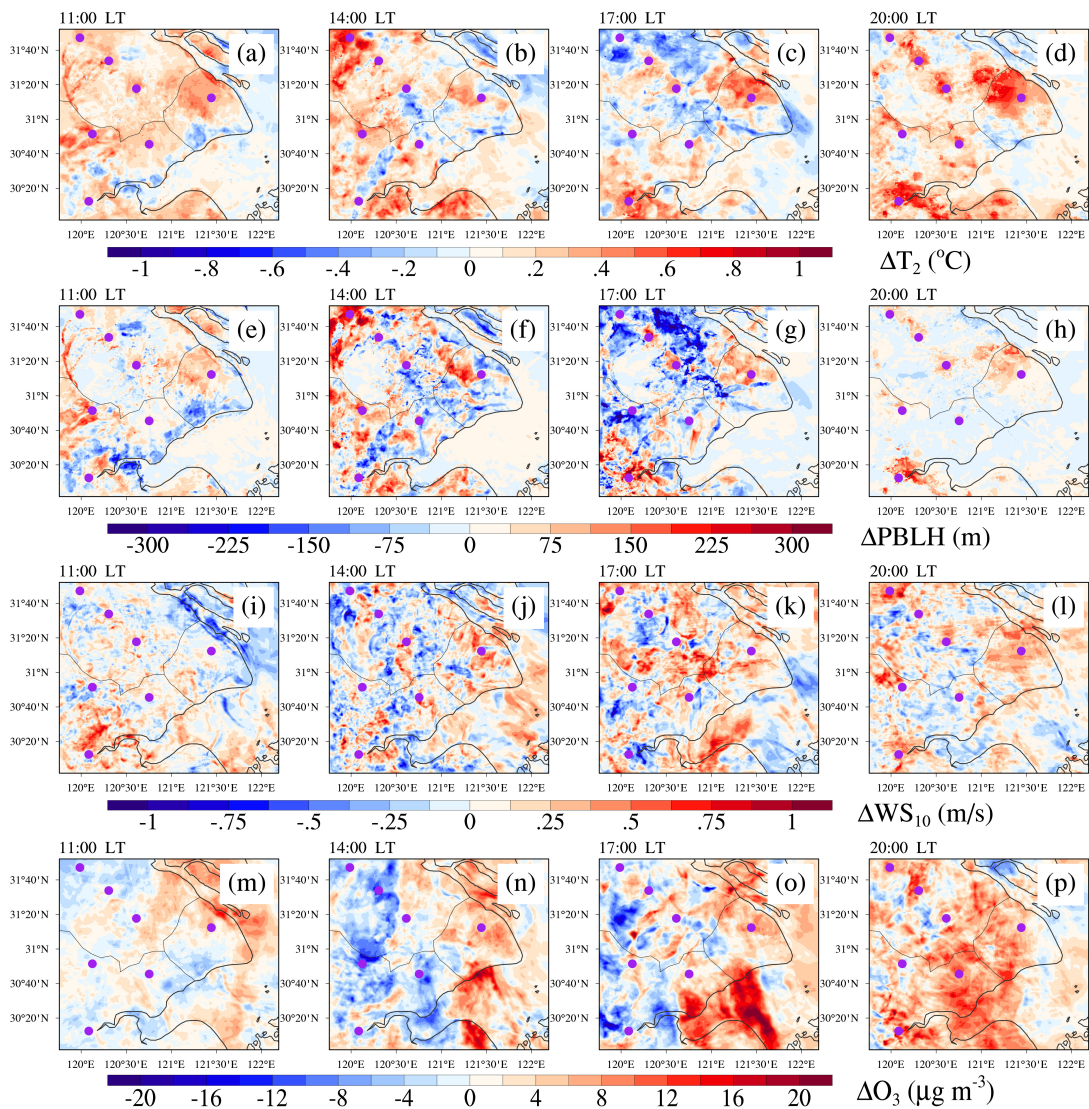
492

493 **3.5 Impacts of anthropogenic heat on meteorology and O₃**

494 **3.5.1 Horizontal changes**

495 Compared with land use, the changes caused by AH are much smaller (Figure 12). Furthermore,
496 these changes are effective in and around cities as they usually have large AH flux densities (Figure
497 3). By adding more surface sensible heat into the atmosphere, the AH fluxes led to an increase

498 in T_2 of $0.2\text{ }^\circ\text{C}$ in urban areas, with a typical value of $0.42\text{ }^\circ\text{C}$ in Shanghai (Figure 12a-d). Vertical
 499 air movement in the boundary layer was then enhanced by the warming of T_2 , and the PBLH
 500 increased as well. According to the simulations, the PBLH increased by $\sim 75\text{ m}$ in the urban areas
 501 (Figure 12e-h). Contrary to the decrease in WS_{10} caused by urban expansion, WS_{10} increased by
 502 $\sim 0.3\text{ m s}^{-1}$ in the urban areas when AH fluxes were taken into account (Figure 12i-l). This is ascribed
 503 to the strengthened urban breeze circulations, which are conducive to the transmission of
 504 momentum from the upper layer to the surface. With regard to surface O_3 concentration, it increased
 505 by $\sim 4\text{ }\mu\text{g m}^{-3}$ in the simulation with adding AH. What's more, the increases in T_2 , PBLH, WS_{10} and
 506 O_3 were clearer after sunset as the solar shortwave radiation disappeared.
 507



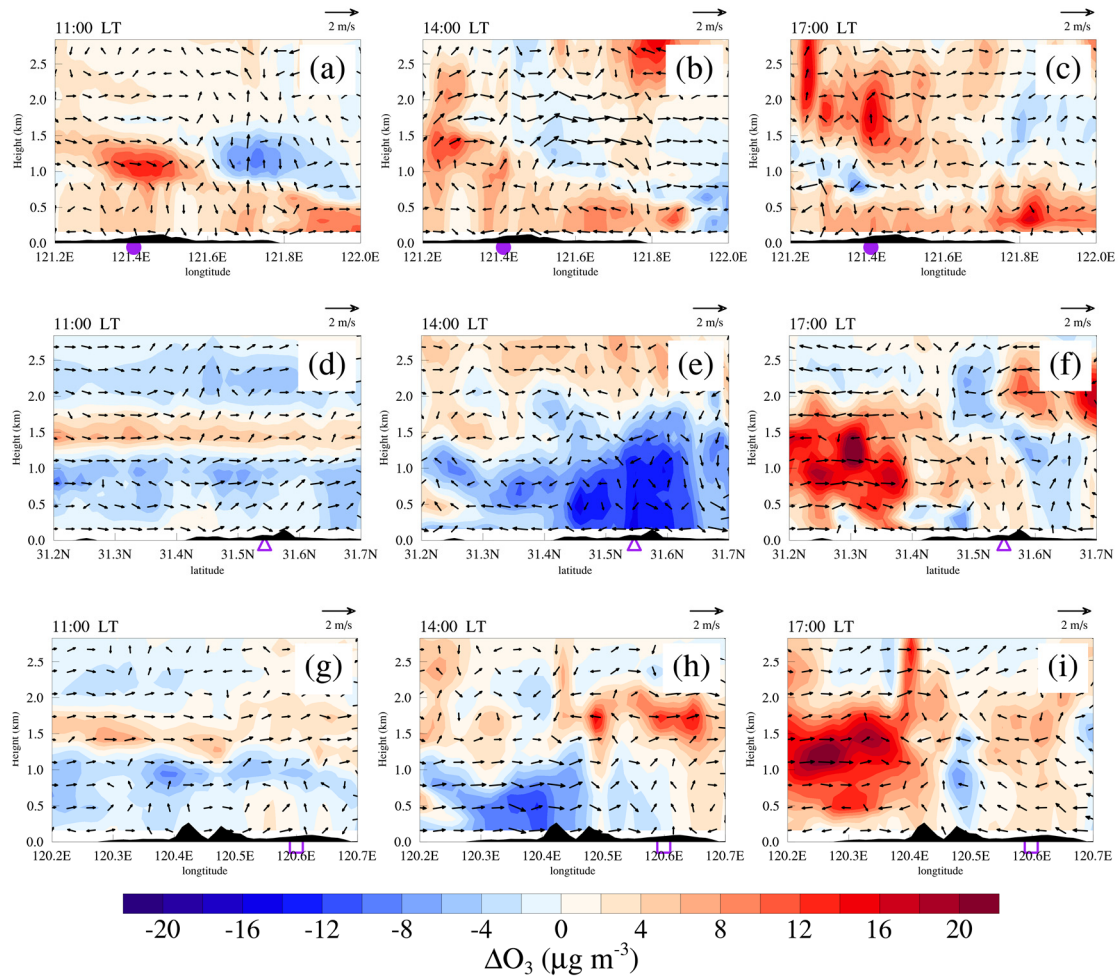
508
 509 **Figure 12.** Same as Figure 10, but for the differences between MODIS_AH and MODIS_noAH
 510 (MODIS_AH – MODIS_noAH).

511

512 **3.5.2 Vertical changes**

513 The phenomenon that cities are almost always warmer than their surroundings is widely known
514 as the urban heat island (UHI), and this urban-rural difference in temperature can further induce the
515 urban heat island circulation (UHIC). There was an enhanced UHIC driven by AH in megacity
516 Shanghai around 14:00 LT (Figure 13b). This circulation extended horizontally 20-30 km from the
517 city center to the urban edge, and vertically to ~2 km from the ground to the top of the urban
518 boundary layer, resulting in a small increase (4~6 $\mu\text{g m}^{-3}$) in surface O_3 . However, for the lakeside
519 cities, the enhanced UHIC was not perceptible. The O_3 concentration in urban areas was reduced on
520 average, with a maximum of 16 $\mu\text{g m}^{-3}$ in Wuxi around 14:00 LT (Figure 13e). The decrease in O_3
521 may be related to the increased wind (Figure 12i-k), which was beneficial to the diffusion and
522 dilution of O_3 . Furthermore, AH has a limited effect on the sea and the lake breezes as it cannot
523 affect any branch of the two as significantly as urban expansion.

524



525

526 **Figure 13.** Same as Figure 9, but for the differences between MODIS_AH and MODIS_noAH
 527 (MODIS_AH – MODIS_noAH).

528

529 3.5.3 The mechanism of anthropogenic heat modulating O₃

530 AH and land use play different roles in meteorology and O₃. AH allows the atmosphere to
 531 reserve more energy via the additional sensible heat fluxes, which increases T₂ by ~0.2 °C. Higher
 532 temperature induces stronger upward air movement to the development of the convective boundary
 533 layer, rising the PBLH by ~75 m. In the convective boundary layer, the atmosphere is associated
 534 with turbulent motions, and is unstable. Together with the enhanced urban breeze caused by AH,
 535 WS₁₀ increases by ~0.3 m s⁻¹. These findings are comparable to the values estimated in other cities
 536 around the world, such as Philadelphia in the United States (Fan and Sailor, 2005), Winnipeg in
 537 Canada (Ferguson and Woodbury, 2007) and Berlin in Germany (Menberg et al., 2013). These
 538 changes in meteorological factors eventually lead to an increase in surface O₃ by ~4 μg m⁻³. It is

539 noteworthy that the effects of AH are usually clearer at night in urban areas. In addition, although
540 AH plays an important role in urban breeze circulations, it may not be powerful enough to affect
541 local circulations such as the sea and the lake breezes.

542

543 **4 Summary and conclusions**

544 Land use change via urban expansion and the increase of AH release are important
545 manifestations of urbanization. They can alter the regional meteorology and thereby affect O₃
546 concentrations in and around cities. In this study, the YRD region, a highly urbanized coastal area
547 with severe O₃ pollution, is selected to investigate this issue. Firstly, the basic characteristics of O₃
548 pollution in the YRD are provided based on the surface observations. Secondly, a representative
549 case is selected for further study using the WRF-Chem model, and the model performance is
550 evaluated by comparing with the observations. Finally, the response of O₃ to changes in meteorology
551 caused by land use and AH are discussed via the model inter-comparisons. The main findings are
552 listed as below:

553 (1) Regional O₃ pollution occurred frequently in the YRD (~26 times per year) from 2015 to
554 2019. These O₃ pollution episodes mainly occur in calm conditions characterized by high
555 temperature (over 20 °C), low relative humidity (less than 80%), light wind (less than 3 m s⁻¹) and
556 shallow cloud cover (less than 5 okta). In this case, the sea and the lake breezes tend to develop and
557 have an important impact on the distribution of O₃ in the YRD.

558 (2) By updating the land use dataset from USGS to MODIS, we find an increase in T₂ by a
559 maximum of 3 °C, an increase in PBLH by a maximum of 500 m and a decrease in WS₁₀ by a
560 maximum of 1.5 m s⁻¹ in the YRD. The higher temperature and PBLH elevate the surface O₃
561 concentration by a maximum of 20 µg m⁻³ via stronger photochemical reactions and vertical mixing
562 processes. Apart from meteorological factors, the sea and the lake breezes are also modified by
563 urban expansion associated with urbanization. The sea breeze is enhanced due to the expansion of
564 coastal cities. Nevertheless, further progression inland of the sea breeze is stalled in the afternoon
565 on account of the rough urban surface, reducing the transmission of O₃ from the coast to the land.
566 The expansion of lakeside cities extends the lifetime of the lake breeze from noon to afternoon.
567 Since the lake breeze accelerates the vertical mixing of O₃ in the boundary layer, the surface O₃ in
568 lakeside cities can increase as much as 30 µg m⁻³.

569 (3) When the AH fluxes are taken into account, T_2 , PBLH, WS_{10} and O_3 will increase by about
570 0.2 °C, 75 m, 0.3 m s^{-1} and $4 \mu\text{g m}^{-3}$ in and around cities, respectively. These changes are relatively
571 smaller compared to urban expansion, and mainly appear around cities where the AH fluxes are
572 large. In addition, unlike urban expansion, AH may have a limited impact on the sea and the lake
573 breezes. But the urban breeze circulations are found to be sensitive to AH inputs.

574 Studying the impacts of land use and AH forced by human activities on urban environment is
575 fundamental in improving the urban air quality. Although this study only focuses on the YRD region,
576 most of the results can be supported by previous studies conducted in other regions around the world.
577 As an increasing number of city clusters composed of large and medium-sized cities are being built,
578 this work can provide valuable insight into the formation of O_3 pollution in rapidly developing
579 regions with unique geographical features.

580

581 ***Data Availability Statement.***

582 Air quality monitoring data were acquired from a mirror of data from the official NEMC real-time
583 publishing platform (<https://quotsoft.net/air/>). Meteorological data were issued by the NCDC
584 (<ftp://ftp.ncdc.noaa.gov/pub/data/noaa/isd-lite/>). The FNL meteorological data were taken from the
585 NCEP (<https://doi.org/10.5065/D6M043C6/>). The MEIC data were accessible at
586 <http://meicmodel.org/>. These data can be downloaded for free as long as you agree to the official
587 instructions.

588

589 ***Author contributions.***

590 CZ and MX had the original ideas, designed the research, collected the data and prepared the original
591 draft. CZ did the numerical simulations and carried out the data analysis. MX acquired financial
592 support for the project leading to this publication.

593

594 ***Competing interests.***

595 The contact author has declared that neither they nor their co-authors have any competing interests.

596

597 ***Acknowledgements.***

598 We are grateful to MEPC for the air quality monitoring data, to NCDC for the meteorological data,

599 to NCEP for global final analysis fields and to Tsinghua University for the MEIC inventories. The
600 numerical calculations were performed on the Blade cluster system in the High Performance
601 Computing and Massive Data Center (HPC&MDC) of School of Atmospheric Sciences, Nanjing
602 University. We also thank the anonymous reviewers for the constructive comments and suggestions.

603

604 ***Financial support.***

605 This work was supported by the Natural Science Foundation of Jiangsu Province (BK20211158)
606 and the National Key Research and Development Program of China (2018YFC0213502,
607 2018YFC1506404, 2019YFA0606803).

608

609 **References**

- 610 Abdi-Oskouei, M., Carmichael, G., Christiansen, M., Ferrada, G., Roozitalab, B., Sobhani, N., Wade,
611 K., Czarnetzki, A., Pierce, R. B., Wagner, T., and Stanier, C.: Sensitivity of Meteorological
612 Skill to Selection of WRF-Chem Physical Parameterizations and Impact on Ozone Prediction
613 During the Lake Michigan Ozone Study (LMOS), *J Geophys Res-Atmos*, 125, 2020.
- 614 Bergin, M. S., West, J. J., Keating, T. J., and Russell, A. G.: Regional atmospheric pollution and
615 transboundary air quality management, *Annu. Rev. Environ. Resour.*, 30, 1-37,
616 10.1146/annurev.energy.30.050504.144138, 2005.
- 617 Blaylock, B. K., Horel, J. D., and Crosman, E. T.: Impact of Lake Breezes on Summer Ozone
618 Concentrations in the Salt Lake Valley, *Journal of Applied Meteorology and Climatology*, 56,
619 353-370, 2017.
- 620 Buchholz, S., Junk, J., Krein, A., Heinemann, G., and Hoffmann, L.: Air pollution characteristics
621 associated with mesoscale atmospheric patterns in northwest continental Europe, *Atmospheric*
622 *Environment*, 44, 5183-5190, 10.1016/j.atmosenv.2010.08.053, 2010.
- 623 Chameides, W., and Walker, J. C. G.: A photochemical theory of tropospheric ozone, *Journal of*
624 *Geophysical Research*, 78, 8751-8760, 10.1029/JC078i036p08751, 1973.
- 625 Chen, F., and Dudhia, J.: Coupling an advanced land surface-hydrology model with the Penn State-
626 NCAR MM5 modeling system. Part II: Preliminary model validation, *Monthly Weather*
627 *Review*, 129, 587-604, 2001.
- 628 Chen, G., Zhao, L., and Mochida, A.: Urban Heat Island Simulations in Guangzhou, China, Using

629 the Coupled WRF/UCM Model with a Land Use Map Extracted from Remote Sensing Data,
630 Sustainability, 8, 10.3390/su8070628, 2016.

631 Chen, S. H., and Sun, W. Y.: A one-dimensional time dependent cloud model, J Meteorol Soc Jpn,
632 80, 99-118, 2002.

633 Crosman, E. T., and Horel, J. D.: Sea and Lake Breezes: A Review of Numerical Studies, Boundary-
634 Layer Meteorology, 137, 1-29, 10.1007/s10546-010-9517-9, 2010.

635 De Meij, A., and Vinuesa, J. F.: Impact of SRTM and Corine Land Cover data on meteorological
636 parameters using WRF, Atmospheric Research, 143, 351-370, 10.1016/j.atmosres.2014.03.004,
637 2014.

638 Ding, A., Wang, T., Zhao, M., Wang, T., and Li, Z.: Simulation of sea-land breezes and a discussion
639 of their implications on the transport of air pollution during a multi-day ozone episode in the
640 Pearl River Delta of China, Atmospheric Environment, 38, 6737-6750,
641 10.1016/j.atmosenv.2004.09.017, 2004.

642 Fan, H. L., and Sailor, D. J.: Modeling the impacts of anthropogenic heating on the urban climate
643 of Philadelphia: a comparison of implementations in two PBL schemes, Atmospheric
644 Environment, 39, 73-84, 2005.

645 Fast, J. D., Gustafson, W. I., Easter, R. C., Zaveri, R. A., Barnard, J. C., Chapman, E. G., Grell, G.
646 A., and Peckham, S. E.: Evolution of ozone, particulates, and aerosol direct radiative forcing
647 in the vicinity of Houston using a fully coupled meteorology-chemistry-aerosol model, J
648 Geophys Res-Atmos, 111, 2006.

649 Ferguson, G., and Woodbury, A. D.: Urban heat island in the subsurface, Geophysical Research
650 Letters, 34, 2007.

651 Flanner, M. G.: Integrating anthropogenic heat flux with global climate models, Geophysical
652 Research Letters, 36, n/a-n/a, 10.1029/2008gl036465, 2009.

653 Freitas, E. D., Rozoff, C. M., Cotton, W. R., and Dias, P. L. S.: Interactions of an urban heat island
654 and sea-breeze circulations during winter over the metropolitan area of Sao Paulo, Brazil,
655 Boundary-Layer Meteorology, 122, 43-65, 2007.

656 Friedl, M. A., Sulla-Menashe, D., Tan, B., Schneider, A., Ramankutty, N., Sibley, A., and Huang,
657 X.: MODIS Collection 5 global land cover: Algorithm refinements and characterization of new
658 datasets, Remote Sensing of Environment, 114, 168-182, 10.1016/j.rse.2009.08.016, 2010.

659 Fu, Y. and Liao, H.: Impacts of land use and land cover changes on biogenic emissions of volatile
660 organic compounds in China from the late 1980s to the mid-2000s: implications for
661 tropospheric ozone and secondary organic aerosol, *Tellus B: Chemical and Physical*
662 *Meteorology*, 66, 10.3402/tellusb.v66.24987, 2014.

663 Gao, D., Xie, M., Chen, X., Wang, T. J., Liu, J., Xu, Q., Mu, X. Y., Chen, F., Li, S., Zhuang, B. L.,
664 Li, M. M., Zhao, M., and Ren, J. Y.: Systematic classification of circulation patterns and
665 integrated analysis of their effects on different ozone pollution levels in the Yangtze River Delta
666 Region, China, *Atmospheric Environment*, 242, 2020.

667 Gong, P., Liu, H., Zhang, M., Li, C., Wang, J., Huang, H., Clinton, N., Ji, L., Li, W., Bai, Y., Chen,
668 B., Xu, B., Zhu, Z., Yuan, C., Ping Suen, H., Guo, J., Xu, N., Li, W., Zhao, Y., Yang, J., Yu, C.,
669 Wang, X., Fu, H., Yu, L., Dronova, I., Hui, F., Cheng, X., Shi, X., Xiao, F., Liu, Q., and Song,
670 L.: Stable classification with limited sample: transferring a 30-m resolution sample set
671 collected in 2015 to mapping 10-m resolution global land cover in 2017, *Science Bulletin*, 64,
672 370-373, 10.1016/j.scib.2019.03.002, 2019.

673 Grell, G. A., and Dévényi, D.: A generalized approach to parameterizing convection combining
674 ensemble and data assimilation techniques, *Geophysical Research Letters*, 29, 38-31-38-34,
675 10.1029/2002gl015311, 2002.

676 Grell, G. A., Peckham, S. E., Schmitz, R., McKeen, S. A., Frost, G., Skamarock, W. C., and Eder,
677 B.: Fully coupled “online” chemistry within the WRF model, *Atmospheric Environment*, 39,
678 6957-6975, 10.1016/j.atmosenv.2005.04.027, 2005.

679 Guenther, A., Karl, T., Harley, P., Wiedinmyer, C., Palmer, P. I., and Geron, C.: Estimates of global
680 terrestrial isoprene emissions using MEGAN (Model of Emissions of Gases and Aerosols from
681 Nature), *Atmospheric Chemistry and Physics*, 6, 3181-3210, 2006.

682 Hong, S. Y., Noh, Y., and Dudhia, J.: A new vertical diffusion package with an explicit treatment of
683 entrainment processes, *Monthly Weather Review*, 134, 2318-2341, 2006.

684 Hu, J., Li, Y., Zhao, T., Liu, J., Hu, X.-M., Liu, D., Jiang, Y., Xu, J., and Chang, L.: An important
685 mechanism of regional O₃ transport for summer smog over the
686 Yangtze River Delta in eastern China, *Atmospheric Chemistry and Physics*, 18, 16239-16251,
687 10.5194/acp-18-16239-2018, 2018.

688 Jacob, D. J., and Winner, D. A.: Effect of climate change on air quality, *Atmospheric Environment*,

689 43, 51-63, 10.1016/j.atmosenv.2008.09.051, 2009.

690 Jerrett, M., Burnett, R. T., Pope, C. A., Ito, K., Thurston, G., Krewski, D., Shi, Y. L., Calle, E., and
691 Thun, M.: Long-Term Ozone Exposure and Mortality., *New Engl J Med*, 360, 1085-1095, 2009.

692 Jiang, X., Wiedinmyer, C., Chen, F., Yang, Z.-L., and Lo, J. C.-F.: Predicted impacts of climate and
693 land use change on surface ozone in the Houston, Texas, area, *Journal of Geophysical Research*,
694 113, 10.1029/2008jd009820, 2008.

695 Jimenez, P. A., and Dudhia, J.: Improving the Representation of Resolved and Unresolved
696 Topographic Effects on Surface Wind in the WRF Model, *Journal of Applied Meteorology and
697 Climatology*, 51, 300-316, 2012.

698 Kim, H.-J., and Wang, B.: Sensitivity of the WRF model simulation of the East Asian summer
699 monsoon in 1993 to shortwave radiation schemes and ozone absorption, *Asia-Pacific Journal
700 of Atmospheric Sciences*, 47, 167-180, 10.1007/s13143-011-0006-y, 2011.

701 Lennartson, G. J., and Schwartz, M. D.: The lake breeze-ground-level ozone connection in eastern
702 Wisconsin: A climatological perspective, *International Journal of Climatology*, 22, 1347-1364,
703 2002.

704 Li, K., Jacob, D. J., Shen, L., Lu, X., De Smedt, I., and Liao, H.: Increases in surface ozone pollution
705 in China from 2013 to 2019: anthropogenic and meteorological influences, *Atmospheric
706 Chemistry and Physics*, 20, 11423-11433, 10.5194/acp-20-11423-2020, 2020.

707 Li, M., Song, Y., Huang, X., Li, J., Mao, Y., Zhu, T., Cai, X., and Liu, B.: Improving mesoscale
708 modeling using satellite-derived land surface parameters in the Pearl River Delta region, China,
709 *Journal of Geophysical Research: Atmospheres*, 119, 6325-6346, 10.1002/2014jd021871,
710 2014.

711 Li, M., Wang, T., Xie, M., Zhuang, B., Li, S., Han, Y., Song, Y., and Cheng, N.: Improved
712 meteorology and ozone air quality simulations using MODIS land surface parameters in the
713 Yangtze River Delta urban cluster, China, *Journal of Geophysical Research: Atmospheres*, 122,
714 3116-3140, 10.1002/2016jd026182, 2017.

715 Li, Y., Zhang, J., Sailor, D. J., and Ban-Weiss, G. A.: Effects of urbanization on regional meteorology
716 and air quality in Southern California, *Atmospheric Chemistry and Physics*, 19, 4439-4457,
717 10.5194/acp-19-4439-2019, 2019.

718 Liao, Z., Gao, M., Sun, J., and Fan, S.: The impact of synoptic circulation on air quality and

719 pollution-related human health in the Yangtze River Delta region, *Sci Total Environ*, 607-608,
720 838-846, 10.1016/j.scitotenv.2017.07.031, 2017.

721 Lin, C. H., Lai, C. H., Wu, Y. L., Lin, P. H., and Lai, H. C.: Impact of sea breeze air masses laden
722 with ozone on inland surface ozone concentrations: A case study of the northern coast of
723 Taiwan, *J Geophys Res-Atmos*, 112, 2007.

724 Liu, M., and Tian, H.: China's land cover and land use change from 1700 to 2005: Estimations from
725 high-resolution satellite data and historical archives, *Global Biogeochemical Cycles*, 24, n/a-
726 n/a, 10.1029/2009gb003687, 2010.

727 Loveland, T. R., Reed, B. C., Brown, J. F., Ohlen, D. O., Zhu, Z., Yang, L., and Merchant, J. W.:
728 Development of a global land cover characteristics database and IGBP DISCover from 1 km
729 AVHRR data, *International Journal of Remote Sensing*, 21, 1303-1330,
730 10.1080/014311600210191, 2000.

731 Lu, X., Hong, J., Zhang, L., Cooper, O. R., Schultz, M. G., Xu, X., Wang, T., Gao, M., Zhao, Y., and
732 Zhang, Y.: Severe Surface Ozone Pollution in China: A Global Perspective, *Environmental
733 Science & Technology Letters*, 5, 487-494, 10.1021/acs.estlett.8b00366, 2018.

734 Mavrakou, T., Philippopoulos, K., and Deligiorgi, D.: The impact of sea breeze under different
735 synoptic patterns on air pollution within Athens basin, *Science of the Total Environment*, 433,
736 31-43, 2012.

737 Menberg, K., Bayer, P., Zosseder, K., Rumohr, S., and Blum, P.: Subsurface urban heat islands in
738 German cities, *Sci Total Environ*, 442, 123-133, 10.1016/j.scitotenv.2012.10.043, 2013.

739 Miao, Y., Hu, X.-M., Liu, S., Qian, T., Xue, M., Zheng, Y., and Wang, S.: Seasonal variation of local
740 atmospheric circulations and boundary layer structure in the Beijing-Tianjin-Hebei region and
741 implications for air quality, *Journal of Advances in Modeling Earth Systems*, 7, 1602-1626,
742 10.1002/2015ms000522, 2015.

743 Mills, G., Hayes, F., Simpson, D., Emberson, L., Norris, D., Harmens, H., and Buker, P.: Evidence
744 of widespread effects of ozone on crops and (semi-)natural vegetation in Europe (1990-2006)
745 in relation to AOT40-and flux-based risk maps, *Glob. Change Biol.*, 17, 592-613,
746 10.1111/j.1365-2486.2010.02217.x, 2011.

747 Mlawer, E. J., Taubman, S. J., Brown, P. D., Iacono, M. J., and Clough, S. A.: Radiative transfer for
748 inhomogeneous atmospheres: RRTM, a validated correlated-k model for the longwave, *Journal*

749 of Geophysical Research: Atmospheres, 102, 16663-16682, 10.1029/97jd00237, 1997.

750 Oke, T. R.; Mills, G.; Christen, A.; Voogt, J. A. Urban Climates; Cambridge University Press:
751 Cambridge, 2017.

752 Park, R. J., Hong, S. K., Kwon, H. A., Kim, S., Guenther, A., Woo, J. H., and Loughner, C. P.: An
753 evaluation of ozone dry deposition simulations in East Asia, Atmospheric Chemistry and
754 Physics, 14, 7929-7940, 10.5194/acp-14-7929-2014, 2014.

755 Ryu, Y.-H., Baik, J.-J., and Lee, S.-H.: Effects of anthropogenic heat on ozone air quality in a
756 megacity, Atmospheric Environment, 80, 20-30, 10.1016/j.atmosenv.2013.07.053, 2013.

757 Sailor, D. J.: A review of methods for estimating anthropogenic heat and moisture emissions in the
758 urban environment, International Journal of Climatology, 31, 189-199, 10.1002/joc.2106, 2011.

759 Sati, A. P., and Mohan, M.: The impact of urbanization during half a century on surface meteorology
760 based on WRF model simulations over National Capital Region, India, Theoretical and Applied
761 Climatology, 134, 309-323, 2017.

762 Schell, B., Ackermann, I. J., Hass, H., Binkowski, F. S., and Ebel, A.: Modeling the formation of
763 secondary organic aerosol within a comprehensive air quality model system, J Geophys Res-
764 Atmos, 106, 28275-28293, 2001.

765 Sills, D. M. L., Brook, J. R., Levy, I., Makar, P. A., Zhang, J., and Taylor, P. A.: Lake breezes in the
766 southern Great Lakes region and their influence during BAQS-Met 2007, Atmospheric
767 Chemistry and Physics, 11, 7955-7973, 10.5194/acp-11-7955-2011, 2011.

768 Stockwell, W. R., Middleton, P., Chang, J. S., and Tang, X. Y.: The 2nd Generation Regional Acid
769 Deposition Model Chemical Mechanism for Regional Air-Quality Modeling, J Geophys Res-
770 Atmos, 95, 16343-16367, 1990.

771 Wang, H., Wu, Q., Liu, H., Wang, Y., Cheng, H., Wang, R., Wang, L., Xiao, H., and Yang, X.:
772 Sensitivity of biogenic volatile organic compound emissions to leaf area index and land cover
773 in Beijing, Atmospheric Chemistry and Physics, 18, 9583-9596, 10.5194/acp-18-9583-2018,
774 2018.

775 Wang, T., Xue, L., Brimblecombe, P., Lam, Y. F., Li, L., and Zhang, L.: Ozone pollution in China:
776 A review of concentrations, meteorological influences, chemical precursors, and effects, Sci
777 Total Environ, 575, 1582-1596, 10.1016/j.scitotenv.2016.10.081, 2017.

778 Wang, X., Chen, F., Wu, Z., Zhang, M., Tewari, M., Guenther, A., and Wiedinmyer, C.: Impacts of

779 weather conditions modified by urban expansion on surface ozone: Comparison between the
780 Pearl River Delta and Yangtze River Delta regions, *Advances in Atmospheric Sciences*, 26,
781 962-972, 10.1007/s00376-009-8001-2, 2009.

782 Wang, Y., Gao, W., Wang, S., Song, T., Gong, Z., Ji, D., Wang, L., Liu, Z., Tang, G., Huo, Y., Tian,
783 S., Li, J., Li, M., Yang, Y., Chu, B., Petäjä, T., Kerminen, V.-M., He, H., Hao, J., Kulmala, M.,
784 Wang, Y., and Zhang, Y.: Contrasting trends of PM_{2.5} and surface-ozone concentrations in
785 China from 2013 to 2017, *National Science Review*, 7, 1331-1339, 10.1093/nsr/nwaa032, 2020.

786 Wentworth, G. R., Murphy, J. G., and Sills, D. M. L.: Impact of lake breezes on ozone and nitrogen
787 oxides in the Greater Toronto Area, *Atmospheric Environment*, 109, 52-60,
788 10.1016/j.atmosenv.2015.03.002, 2015.

789 Xie, M., Liao, J., Wang, T., Zhu, K., Zhuang, B., Han, Y., Li, M., and Li, S.: Modeling of the
790 anthropogenic heat flux and its effect on regional meteorology and air quality over the Yangtze
791 River Delta region, China, *Atmospheric Chemistry and Physics*, 16, 6071-6089, 10.5194/acp-
792 16-6071-2016, 2016a.

793 Xie, M., Shu, L., Wang, T.-j., Liu, Q., Gao, D., Li, S., Zhuang, B.-l., Han, Y., Li, M.-m., and Chen,
794 P.-l.: Natural emissions under future climate condition and their effects on surface ozone in the
795 Yangtze River Delta region, China, *Atmospheric Environment*, 150, 162-180,
796 10.1016/j.atmosenv.2016.11.053, 2017.

797 Xie, M., Zhu, K., Wang, T., Feng, W., Gao, D., Li, M., Li, S., Zhuang, B., Han, Y., Chen, P., and
798 Liao, J.: Changes in regional meteorology induced by anthropogenic heat and their impacts on
799 air quality in South China, *Atmospheric Chemistry and Physics*, 16, 15011-15031,
800 10.5194/acp-16-15011-2016, 2016b.

801 Xie, M., Zhu, K., Wang, T., Yang, H., Zhuang, B., Li, S., Li, M., Zhu, X., and Ouyang, Y.:
802 Application of photochemical indicators to evaluate ozone nonlinear chemistry and pollution
803 control countermeasure in China, *Atmospheric Environment*, 99, 466-473,
804 10.1016/j.atmosenv.2014.10.013, 2014.

805 You, C., Fung, J. C. H., and Tse, W. P.: Response of the Sea Breeze to Urbanization in the Pearl
806 River Delta Region, *Journal of Applied Meteorology and Climatology*, 58, 1449-1463, 2019.

807 Young, P. J., Archibald, A. T., Bowman, K. W., Lamarque, J. F., Naik, V., Stevenson, D. S., Tilmes,
808 S., Voulgarakis, A., Wild, O., Bergmann, D., Cameron-Smith, P., Cionni, I., Collins, W. J.,

809 Dalsøren, S. B., Doherty, R. M., Eyring, V., Faluvegi, G., Horowitz, L. W., Josse, B., Lee, Y.
810 H., MacKenzie, I. A., Nagashima, T., Plummer, D. A., Righi, M., Rumbold, S. T., Skeie, R. B.,
811 Shindell, D. T., Strode, S. A., Sudo, K., Szopa, S., and Zeng, G.: Pre-industrial to end 21st
812 century projections of tropospheric ozone from the Atmospheric Chemistry and Climate Model
813 Intercomparison Project (ACCMIP), *Atmospheric Chemistry and Physics*, 13, 2063-2090,
814 10.5194/acp-13-2063-2013, 2013.

815 Yu, M., Carmichael, G. R., Zhu, T., and Cheng, Y.: Sensitivity of predicted pollutant levels to
816 urbanization in China, *Atmospheric Environment*, 60, 544-554,
817 10.1016/j.atmosenv.2012.06.075, 2012.

818 Zhan, C., Xie, M., Huang, C., Liu, J., Wang, T., Xu, M., Ma, C., Yu, J., Jiao, Y., Li, M., Li, S.,
819 Zhuang, B., Zhao, M., and Nie, D.: Ozone affected by a succession of four landfall typhoons
820 in the Yangtze River Delta, China: major processes and health impacts, *Atmospheric Chemistry
821 and Physics*, 20, 13781-13799, 10.5194/acp-20-13781-2020, 2020.

822 Zhan, C., Xie, M., Liu, J., Wang, T., Xu, M., Chen, B., Li, S., Zhuang, B., and Li, M.: Surface Ozone
823 in the Yangtze River Delta, China: A Synthesis of Basic Features, Meteorological Driving
824 Factors, and Health Impacts, *Journal of Geophysical Research: Atmospheres*, 126,
825 10.1029/2020jd033600, 2021.

826 Zhan, C.-c., Xie, M., Fang, D.-x., Wang, T.-j., Wu, Z., Lu, H., Li, M.-m., Chen, P.-l., Zhuang, B.-l.,
827 Li, S., Zhang, Z.-q., Gao, D., Ren, J.-y., and Zhao, M.: Synoptic weather patterns and their
828 impacts on regional particle pollution in the city cluster of the Sichuan Basin, China,
829 *Atmospheric Environment*, 208, 34-47, 10.1016/j.atmosenv.2019.03.033, 2019.

830 Zhang, N., Zhu, L., and Zhu, Y.: Urban heat island and boundary layer structures under hot weather
831 synoptic conditions: A case study of Suzhou City, China, *Advances in Atmospheric Sciences*,
832 28, 855-865, 10.1007/s00376-010-0040-1, 2011.

833 Zhang, H., Wang, Y., Hu, J., Ying, Q., and Hu, X. M.: Relationships between meteorological
834 parameters and criteria air pollutants in three megacities in China, *Environ Res*, 140, 242-254,
835 10.1016/j.envres.2015.04.004, 2015.

836 Zhu, B., Kang, H., Zhu, T., Su, J., Hou, X., and Gao, J.: Impact of Shanghai urban land surface
837 forcing on downstream city ozone chemistry, *Journal of Geophysical Research: Atmospheres*,
838 120, 4340-4351, 10.1002/2014jd022859, 2015.

